Low Complexity Residual Doppler Shift Estimation for Underwater Acoustic Multicarrier Communication

Alon Amar, *Member, IEEE*, Gilad Avrashi, *Student Member, IEEE*, and Milica Stojanovic, *Fellow, IEEE*

***Abstract*—We propose two computationally efficient residual Doppler shift estimation methods for underwater acoustic multicarrier communication. The first method is based on computing the phase of the root of a low order polynomial. The second method is a closed-form least squares estimate given the unwrapped phases of the minimal eigenvector of a small data matrix. The complexities of both estimates are significantly lower compared to the methods commonly used in underwater acoustic multicarrier communication, which result in nonlinear least squares estimators and thus require a fine grid search in the frequency domain. Numerical simulations show that the mean square errors of the proposed methods have similar performance as the common estimation techniques, achieve the Cramer–Rao lower bounds at low noise levels, and agree with their theoretically derived variances. Pool experiments and sea trial results further demonstrate that the suggested estimates yield similar results as the common nonlinear least squares estimates but at a lower complexity.**

***Index Terms*—Underwater acoustic communication, orthogonal frequency division multiplexing, carrier frequency offset.**

I. Introduction

THE problem of estimating the carrier frequency offset (CFO) continues to be a research subject with significant importance for communication systems [1]–[4]. Specifically, in the current work we concentrate on CFO estimation for orthogonal frequency division multiplexing (OFDM) in underwater acoustic communication (UAC). The time-variations of the underwater acoustic channel may cause non-uniform Doppler shifts that result in loss of orthogonality between the OFDM carriers and in turn may increase the decoding errors [7]–[9], [11]. Usually the processing at the receiver side in UAC OFDM systems consists of two steps to mitigate this loss of orthogonality [7]: First, compensating for the coarse Doppler shift by resampling the received signals. Second, estimating the residual Doppler shift (i.e., the CFO) given the resampled signal. Herein, we assume that the first step has been performed, and only focus on the second step.

While in radio communication it is possible to estimate the CFO using synchronization blocks [13]–[15], [23] (possibly designed under optimality criterion such as the Cramer-Rao lower bound (CRLB) [6]), and then compensate the subsequent received data, or to employ blind CFO estimators [5], [16]–[22], [24] that only rely on the received data, such approaches are usually not practical in UAC due to its unique channel characteristics [25]. For example, the frequency bandwidth of the underwater acoustic channel is limited and thus each block is used for data transmission.

There are two common CFO estimation approaches in UAC OFDM [9]–[11] using block-by-block processing, that is, based on processing each block individually. The approach in [9], [10] suggests a non-linear least squares (NLS) CFO estimate using Q randomly selected pilot symbols in each block with equal spacing $G = K/Q$ (usually between 4 to 8) in the frequency domain, where K is the number of block carriers. These pilot symbols are also used to estimate the channel impulse response (CIR). Such an approach requires a fine grid search in the frequency domain and the number of multiplications involved in its computation increases with respect to (w.r.t.) $\sqrt{K}G$, which depends on the number of carriers. The second approach [11] also proposes a NLS-based CFO estimate with a similar computation load as in [9]; however, the approach in [11] suggests using null symbols in the frequency domain to estimate the CFO, while pilot symbols are used to estimate the CIR. As a result, the data rate using this approach is lower than that of the first approach. A block-to-block processing approach for UAC OFDM systems is suggested in [12], where the non-uniform phase offset is tracked from one block to the subsequent block.

Herein, we suggest a CFO estimate based on block-by-block processing that achieves a similar estimation error as that of the estimates presented in [9], [11] but the number of multiplications involved in their computations increases w.r.t. G^2, which is small in practice. Such a reduction is important in practice as UAC OFDM systems are usually limited in power and also limited in their signal processing resources. The proposed design uses the same number of pilot symbols as in [9], [11] with the same spacing G in the frequency domain. However, contrary to

Manuscript received May 17, 2016; revised September 25, 2016; accepted October 27, 2016. Date of publication November 17, 2016; date of current version February 7, 2017. The associate editor coordinating the review of this manuscript and approving it for publication is Dr. Ashish Pandharipande. The work of M. Stojanovic was supported by the ONR Grant (N00014-15-1-2550) and the NSF Grant (CNS-1212999).

A. Amar and G. Avrashi are with the Department of Electrical Engineering, Technion Israel institute of technology, Haifa 32000, Israel (e-mail: aamar@techunix.technion.ac.il; avrgilad@gmail.com).

M. Stojanovic is with the Department of Electrical and Computer Engineering, Northeastern University, Boston, MA 02115 USA (e-mail: millitsa@ece.neu.edu).

Color versions of one or more of the figures in this paper are available online at http://ieeexplore.ieee.org.

Digital Object Identifier 10.1109/TSP.2016.2630039

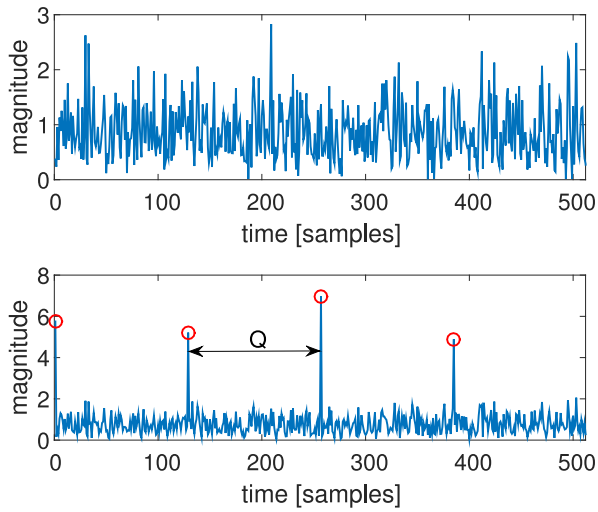

Fig. 1. An OFDM block in the time-domain with $K = 512$ carriers (each symbol is selected from a quadrature phase shift keying (QPSK) constellation) and $Q = 128$ pilot symbols selected at random (upper plot) and using identical pilot symbols (bottom plot).

[9], [11], all the Q pilot symbols in the proposed design are identical. As a result, every Q time samples, the identical symbols are summed coherently (the peak to average power ratio (PAPR) of such a data block is discussed later). Since the other $K - Q$ data symbols are selected randomly, at any time sample their sum can be treated as an additive noise (see Fig. 1).

By using such a pilot symbols design we actually construct an OFDM block which is composed of a sequence of G identical segments, each of which is immersed in noise. Whereas the CFO estimate in case of random pilot symbols uses all the time samples of the block together and results in an exhaustive-search in the CFO space, the proposed periodic structure can be exploited to estimate the CFO in an efficient manner. For example, one can compute the phase arguments of the inner-products between all pairs of segments, and then determine the CFO by combining these phases together, e.g., in a least squares (LS) sense, or simply focus on the one with the highest signal to noise ratio (SNR). The notion of estimating the CFO based on cross correlating time sequences of OFDM blocks is also proposed in [13], [14] for radio communication. In [13] Q pseudo-random pilot carriers are spread uniformly over the frequency domain. The CFO is estimated by computing the phase of the summation of the products between the frequency responses at the Q carriers at one OFDM block and the conjugate of the frequency responses at the same Q carriers at a different OFDM block. Such an operation is equivalent to cross correlating the two distinct time sequences where each one is obtained by transforming the pseudo-random pilot carriers of an OFDM block to time. A similar method is suggested in [14] where the pilot set is placed in a training block such that its two halves are present within the same OFDM block. The assumption behind the approach in [13] is that the CFO remains the same over several OFDM blocks, while in [14] a training block is used to estimate the CFO and then this estimate is used for the subsequent OFDM blocks. As previously discussed both assumptions do not hold in UAC due the time varying characteristics of the channel.

Instead of computing the argument of the product of each pair of segments independently, we organize the complete set of these $G(G-1)/2$ segments inner-products into a small Hermitian $G \times G$ matrix which is then used to derive two low-complexity CFO estimation methods. In the first method, we show that the entries of this matrix are the coefficients of a $2G-1$ polynomial, and the CFO estimate is obtained by computing the argument of the root which is closest to one. In the second method, we provide a closed-form LS CFO estimate which depends on the unwrapped phases of the eigenvector associated with the minimal eigenvalue of this small $G \times G$ data matrix.

We emphasize that from our perspective besides developing new CFO estimators for OFDM communications in underwater acoustic channel, these estimates require considerably less computational complexity compared to previously suggested CFO estimates while maintaining similar estimation accuracy. Specifically, as we show later, while the computational complexity of previously suggested exhaustive-based CFO estimates increases w.r.t. $\sqrt{K}G$, the computational complexities of the proposed estimates only increases w.r.t. G^2, which is a considerable computation complexity reduction.

The numerical simulation results indicate that the root mean square error (RMSE) performance of the proposed CFO and channel estimates are similar to those of the common NLS-based CFO estimates [9], [11], and that the RMSE's converge to the CRLB for large SNR. Pool experiments and sea trial results further indicate that the suggested low-complexity CFO estimates have similar results as the common NLS-based CFO estimates.

II. The ZP-OFDM Signal Model

We consider a zero-padding orthogonal frequency division multiplexing (ZP-OFDM) block with time duration T and K carriers, where the kth carrier frequency is,

$$f(k) = f_0 + k\Delta f\,, k = 0, \ldots, K-1\,, \tag{1}$$

with f_0 the lower frequency, and $\Delta f = 1/T$ is the carrier spacing. The bandwidth is $W = K\Delta f = K/T$. Let the $K \times 1$ vector of symbols be

$$\mathbf{s} = [s(0), s(1), \ldots, s(K-1)]^T\,, \tag{2}$$

where $s(k) = e^{j\phi(k)}$ with $\phi(k) \in \mathcal{S}$ and $\mathcal{S}$ is a pre-defined set of phases, e.g., QPSK constellation. We use Q pilot symbols, equi-spaced in frequency with spacing $G = K/Q$, i.e., according to (1) the frequency of the qth pilot carrier is $f(qG)$, $q = 0, 1, \ldots, Q-1$. The remaining $K - Q$ carriers are with data symbols. The $P \times 1$ zero-padded discrete time transmitted signal, where $P = K + L$, is $\mathbf{r} = \mathbf{T}_{zp}\mathbf{F}_K^H\mathbf{s}$, where $\mathbf{F}_K$ is a $K \times K$ Fourier matrix with the (m,n)th element given by $\frac{1}{\sqrt{K}}e^{-j2\pi/K \cdot mn}$, $\mathbf{T}_{zp} = [\mathbf{I}_K\,, \mathbf{0}_K\,\mathbf{0}_L^T]^T$ is a $P \times K$ zero-padding matrix, $\mathbf{I}_n$ is the $n \times n$ identity matrix, $\mathbf{0}_n$ is a $n \times 1$ vector of zero elements, and L is the length of the zero-padding. We assume that the unknown discrete-time baseband CIR is described by the $L \times 1$ vector

$$\mathbf{h} = [h(0), h(1), \ldots, h(L-1)]^T\,, \tag{3}$$

where L is the delay spread of the channel normalized by the sampling interval,[1] $T_s = T/K$. The CIR vector, $\mathbf{h}$, represents a multipath frequency-selective channel [11]. After coarse Doppler shift compensation, it is assumed that the $P \times 1$ received vector $\mathbf{y} = [y(0), \ldots, y(P-1)]^T$ may still consist a frequency independent residual Doppler shift component, and has the following structure [11], [26]

$$\mathbf{y} = \underbrace{\mathbf{\Gamma}_K(\epsilon_0)\mathbf{H}\mathbf{T}_{zp}\mathbf{F}_K^H\mathbf{s}}_{\triangleq \mathbf{y}_0} + \mathbf{n}\,, \tag{4}$$

where $\mathbf{y}_0$ is the noise-free received signal, $\mathbf{H}$ is a $P \times P$ Toeplitz matrix with first column and first row given by $[\mathbf{h}^T, \mathbf{0}_{P-L}^T]^T$ and $[h(0), \mathbf{0}_{P-1}^T]^T$, respectively, $\mathbf{n} = [n(0), n(1), \ldots, n(P-1)]^T$ is a $P \times 1$ vector representing the additive noise, which for simplicity we assume is modeled as a zero-mean circular complex white Gaussian with covariance matrix $\sigma_n^2\mathbf{I}_P$. Also, given the CFO ε_0 (measured in Hertz) we define the normalized CFO as $\epsilon_0 = \varepsilon_0/\Delta f$. The $P \times P$ matrix $\mathbf{\Gamma}_K(\epsilon_0)$ is defined as

$$\begin{aligned}\mathbf{\Gamma}_K(\epsilon_0) &= \mathrm{diag}(1, e^{j\varepsilon_0 T_s}, \ldots, e^{j\varepsilon_0 T_s(P-1)}),\\ &= \mathrm{diag}(1, e^{j\frac{\varepsilon_0}{\Delta f}\Delta f T_s}, \ldots, e^{j\frac{\varepsilon_0}{\Delta f}\Delta f T_s(P-1)}),\\ &= \mathrm{diag}(1, e^{j\frac{\epsilon_0}{K}}, \ldots, e^{j\frac{\epsilon_0}{K}(P-1)}),\end{aligned} \tag{5}$$

where in the second transition we divided and multiplied the term of each exponential by Δf, and in the third transition we used the fact that $\Delta f T_s = 1/K$.

Given the received signal, $\mathbf{y}$, our goal is to decode the data symbols vector $\mathbf{s}$ given that the normalized CFO, ϵ_0, and the CIR, $\mathbf{h}$, are unknown.

III. The Measurement Data

In order to compensate for the CFO in (4), we pre-multiply $\mathbf{y}$ by $\mathbf{\Gamma}^H(\epsilon)$, where ϵ is a hypothesized normalized CFO in a pre-defined interval. We use a $K \times P$ overlap-and-add matrix $\mathbf{R}_{\text{ola}} = [\mathbf{I}_K, \mathbf{I}_K(:, 1:L)]$, where $\mathbf{I}_K(:, 1:L)$ represents a $K \times L$ matrix with the first L columns of $\mathbf{I}_K$. By pre-multiplying $\mathbf{\Gamma}_K^H(\epsilon)\mathbf{y}$ by $\mathbf{R}_{\text{ola}}$, the last L elements of $\mathbf{\Gamma}_K^H(\epsilon)\mathbf{y}$ are added to the first L elements of $\mathbf{\Gamma}_K^H(\epsilon)\mathbf{y}$. This means that $\mathbf{R}_{\text{ola}}\mathbf{\Gamma}_K^H(\epsilon)\mathbf{y}$ is treated as a circular convolution between the transmitted signal and the channel. Thus, we can get a multiplicative model in the frequency domain. We transform $\mathbf{R}_{\text{ola}}\mathbf{\Gamma}_K^H(\epsilon)\mathbf{y}$ to the frequency domain by pre-multiplying it from the left by $\mathbf{F}_K$. Finally, we use a $Q \times K$ selection matrix to focus on the known pilot symbols at the Q pilot carriers,

$$\mathbf{T}_{sc} = \mathbf{I}_K(1:G:K, :)\,, \tag{6}$$

which is composed of the Q rows of $\mathbf{I}_K$ associated with the pilot symbols indices We thus obtain the $Q \times 1$ measurement vector given as

$$\begin{aligned}\mathbf{x}(\epsilon) &= \mathbf{T}_{sc}\mathbf{F}_K\mathbf{R}_{\text{ola}}\mathbf{\Gamma}_K^H(\epsilon)\mathbf{y}\,,\\ &= \mathbf{F}_Q\mathbf{\Gamma}_Q^H(\epsilon)\mathbf{Y}\alpha(\epsilon)\,,\end{aligned} \tag{7}$$

[1]In practice, prior measurements indicate the delay spread of the channel and we can set the CIR length to L. Thus, to avoid inter-block interference, we set the zero padding length to be equal to the channel length.

where the second transition is detailed in Appendix A. The matrix $\mathbf{F}_Q$ is the $Q \times Q$ Fourier transform matrix (i.e., its (m,n)th element given by $\frac{1}{\sqrt{Q}}e^{-j\frac{2\pi}{Q}\cdot m\,n}$), the $Q \times G$ matrix $\mathbf{Y}$ is obtained by reshaping the $K \times 1$ vector $\mathbf{R}_{\text{ola}}\mathbf{y}$ into a matrix as,

$$\mathbf{Y} = [[\mathbf{R}_{\text{ola}}\mathbf{y}](1:Q), \cdots, [\mathbf{R}_{\text{ola}}\mathbf{y}](K-Q+1:K)]\,, \tag{8}$$

where for example $[\mathbf{R}_{\text{ola}}\mathbf{y}](1:Q)$ represents the first Q elements of $\mathbf{R}_{\text{ola}}\mathbf{y}$ (in MATLAB syntax). We also define the $G \times 1$ unit-norm vector

$$\alpha(\epsilon) = \frac{1}{\sqrt{G}}[1, e^{-j\frac{2\pi}{G}\epsilon}, \ldots, e^{-j\frac{2\pi}{G}(G-1)\epsilon}]^T\,. \tag{9}$$

Assuming that the hypothesized CFO is close to the true CFO such that $\mathbf{\Gamma}_K(\epsilon) \cong \mathbf{\Gamma}_K(\epsilon_0)$ and substituting this approximation in (7) yields that $\mathbf{x}(\epsilon)$ is approximated as

$$\begin{aligned}\mathbf{x}(\epsilon) &\cong \underbrace{\mathbf{T}_{sc}\mathbf{F}_K\mathbf{R}_{\text{ola}}\mathbf{H}\mathbf{T}_{zp}\mathbf{F}_K^H\mathbf{s}}_{=\mathrm{diag}(\bar{\mathbf{h}})} + \underbrace{\mathbf{T}_{sc}\mathbf{F}_K\mathbf{R}_{\text{ola}}\mathbf{\Gamma}_K^H(\epsilon_0)\mathbf{n}}_{\triangleq \boldsymbol{\eta}}\,,\\ &= \underbrace{\mathbf{T}_{sc}\mathrm{diag}(\mathbf{s})\mathbf{T}_{sc}^T}_{\triangleq \mathbf{D}_p}\mathbf{T}_{sc}\bar{\mathbf{h}} + \boldsymbol{\eta}\,,\\ &= \mathbf{D}_p\mathbf{F}_Q(:, 1:L)\mathbf{h} + \boldsymbol{\eta}\,,\end{aligned} \tag{10}$$

where in the first transition in (10) we used the fact that $\mathbf{R}_{\text{ola}}\mathbf{H}\mathbf{T}_{zp}$ is a circulant matrix, and thus it is diagonalized by the Fourier transform matrix $\mathbf{F}_K$ resulting in the diagonal matrix $\mathrm{diag}(\bar{\mathbf{h}})$, where $\bar{\mathbf{h}} = \mathbf{F}_K(:, 1:L)\mathbf{h}$ is the $K \times 1$ frequency response vector of the CIR $\mathbf{h}$. Also in the second transition in (10) we define the $Q \times Q$ diagonal matrix $\mathbf{D}_p$ that contains the pilot symbols on the diagonal. Note that in the second transition, we insert the matrix $\mathbf{T}_{sc}^T\mathbf{T}_{sc}$ which is a $K \times K$ diagonal matrix with all elements equal zero except the Q elements on the main diagonal which equal to one and are associated with the pilot symbols indices (i.e., 1st, Gth, $2G$th rows, etc.). This matrix can be used on the grounds that $\mathbf{T}_{sc}\mathrm{diag}(\mathbf{s})$ has non-zero elements only at the 1st, Gth, $2G$th columns, etc. Finally, at the third transition we used the definition of $\mathbf{T}_{sc}$ in (6) to further express the product $\mathbf{T}_{sc}\mathbf{F}_K\bar{\mathbf{h}}$.

IV. NLS-Based CFO Estimator

The NLS estimation makes no assumptions about the distribution of the noise. As the observation vector $\mathbf{x}(\epsilon)$ is a nonlinear function of ϵ, a nonlinear least squares estimation approach is used. The CFO and the CIR are determined as ϵ and $\mathbf{h}$ that minimize the Euclidean squared distance between $\mathbf{x}(\epsilon)$ in (7) and its approximation in (10), i.e.,

$$L(\epsilon, \mathbf{h}) = \|\mathbf{x}(\epsilon) - \mathbf{D}_p\mathbf{F}_Q(:, 1:L)\mathbf{h}\|^2\,. \tag{11}$$

In Appendix B we derive the CRLB on the estimate of the CFO and the CIR given the observation vector $\mathbf{y}$, which set bounds on the lowest achievable variances of the estimates.

Taking the derivative of (11) w.r.t. $\mathbf{h}$, equating the result to zero, and using the fact that $\mathbf{D}_p^H\mathbf{D}_p = \mathbf{I}_Q$ and $\mathbf{F}_Q^H(:, 1:L)\mathbf{F}_Q(:, 1:L) = \mathbf{I}_L$, yields that the LS estimate of the channel response is

$$\hat{\mathbf{h}} = \mathbf{F}_Q^H(:, 1:L)\mathbf{D}_p^H\mathbf{x}(\epsilon)\,. \tag{12}$$

Notice that (12) can be computed efficiently using the discrete Fourier transform (DFT). Substituting (12) into (11) yields that the estimate of the CFO is given by selecting ϵ that minimizes the quadratic form,

$$\begin{aligned}\ell(\epsilon) &= \mathbf{x}^H(\epsilon)\mathbf{D}_p(\mathbf{I}_Q - \mathbf{F}_Q(:,1:L)\mathbf{F}_Q^H(:,1:L))\mathbf{D}_p^H\mathbf{x}(\epsilon), \\ &= \|\mathbf{Y}\alpha(\epsilon)\|^2 - \|\mathbf{F}_Q^H(:,1:L)\mathbf{D}_p^H\mathbf{F}_Q\mathbf{\Gamma}_Q^H(\epsilon)\mathbf{Y}\alpha(\epsilon)\|^2\,, \end{aligned} \tag{13}$$

where the second transition is obtained by using (7). The estimate in (13) requires a fine grid search over a pre-defined space of ϵ. As we show in Section VII this estimation process results in $\mathcal{O}(K\sqrt{K})$ multiplications and thus the computation load increases significantly with the number of carriers. This increased computation load is the motivation to derive new low-complexity CFO estimates.

V. Root-Based CFO Estimator

The cost function in (13) reveals an interesting fact: The first term in (13) is affected only by the G elements of $\alpha(\epsilon)$. As a result, this first term can be written as a polynomial in $e^{-j\frac{2\pi}{G}\epsilon}$ of order $2G-1$. However, as the second term in (13) contains the product $\mathbf{\Gamma}_Q^H(\epsilon)\mathbf{Y}\alpha(\epsilon)$, it is affected by all K elements of the diagonal matrix $\mathbf{\Gamma}_K^H(\epsilon)$. As a result, this second term can be written as a polynomial in $e^{-j\frac{2\pi}{K}\epsilon}$ of order $2K-1$. This large polynomial order naturally increases the computational complexity of the estimation process. The reason for this increased polynomial order is the presence of the pilot matrix $\mathbf{D}_p$. Hence, our idea is to properly select the pilot symbols such that the polynomial order is significantly reduced. A possible option that we suggest in this work is to select identical pilot symbols, i.e.,

$$\mathbf{D}_p = u\mathbf{I}_Q\,,\, u \in \mathcal{S}\,. \tag{14}$$

For such a selection the product $\mathbf{F}_Q^H(:,1:L)\mathbf{D}_p^H\mathbf{F}_Q = u\mathbf{F}_Q[\mathbf{I}(:,1:L), \mathbf{0}_Q\mathbf{0}_{Q-L}^T]$. Since $|u|=1$ and $\mathbf{\Gamma}_Q(\epsilon)\mathbf{\Gamma}_Q^H(\epsilon) = \mathbf{I}_Q$ we obtain after simple algebraic steps that the cost function in (13) is then expressed as

$$\begin{aligned}\ell(\epsilon) &= \left\| \begin{bmatrix} \mathbf{Y}(1:L,:) \\ \mathbf{Y}(L+1:Q,:) \end{bmatrix} \alpha(\epsilon) \right\|^2 - \|\mathbf{Y}(1:L,:)\alpha(\epsilon)\|^2\,, \\ &= \|\mathbf{Y}(L+1:Q,:)\alpha(\epsilon)\|^2\,. \end{aligned} \tag{15}$$

The mean and variance of such an estimate are detailed in Appendix C. We can still apply a grid search to (15) in a pre-defined space of ϵ to determine the CFO. Such a solution can be termed as a NLS-based method for identical pilot set. However, we next show that for identical pilot selection this is unnecessary and we suggest techniques with lower complexity.

Minimizing (15) is equivalent to minimizing

$$\ell_1(\epsilon) = \alpha^H(\epsilon)\hat{\mathbf{R}}\alpha(\epsilon)\,. \tag{16}$$

The $G \times G$ matrix $\hat{\mathbf{R}}$ is given by

$$\begin{aligned}\hat{\mathbf{R}} &= \frac{1}{Q-L}\mathbf{Y}^H(L+1:Q,:)\mathbf{Y}(L+1:Q,:)\,, \\ &= \begin{bmatrix} \rho_{0,0} & \cdots & \rho_{0,G-1} \\ \rho_{1,0} & \cdots & \rho_{1,G-1} \\ \vdots & \ddots & \vdots \\ \rho_{G-1,0} & \cdots & \rho_{G-1,G-1} \end{bmatrix}, \end{aligned} \tag{17}$$

where we define the correlation coefficient $\rho_{g,g'}$ for $g, g' \in \{0,1,\ldots,G-1\}$ as

$$\begin{aligned}\rho_{g,g'} = \frac{1}{Q-L}&\mathbf{y}(gQ+L+1:gQ+Q)^H \\ &\times \mathbf{y}(g'Q+L+1:g'Q+Q) \end{aligned} \tag{18}$$

Normalization by $Q-L$ in (17) is only necessary for the small error analysis part. Notice that we take the $K\times 1$ observed vector $\mathbf{y}$ (after overlapping and adding), partition it into G segments, retain only the $Q-L$ last elements of each segment, and compute all $(G-1)G/2$ normalized cross-correlations to obtain $\hat{\mathbf{R}}$. This matrix is then used as the measurement matrix.

The cost function (16) can be expressed as a polynomial in $\alpha = e^{-j\frac{2\pi}{G}\epsilon}$ of order $2G-1$, which can be expressed as,

$$\begin{aligned}\ell_1(\epsilon) &= \sum_{i,j=0}^{G-1}\alpha^{j-i}\rho_{i,j}\,, \\ &\overset{m=j-i}{=} \sum_{m=-(G-1)}^{G-1}\alpha^m\sum_{j=0}^{G-1}\rho_{j-m,i}\,, \\ &= \sum_{m=-(G-1)}^{G-1}\alpha^m\underbrace{\sum_{j=\max(m,0)}^{\min(G-1+m,G-1)}\rho_{j-m,i}}_{\triangleq c_m}\,, \end{aligned} \tag{19}$$

where in the third transition we used the possible range values of the index j, i.e., for ρ_j we have $0 \le j \le G-1$ while for ρ_{j-m} we have $m \le j \le G-1+m$, which means that the two intervals exist together when $\max(m,0) \le \min(G-1+m, G-1)$. The mth coefficient c_m is the sum of the mth diagonal of $\hat{\mathbf{R}}$ (e.g., c_0, c_{-1}, c_1 are associated with the main diagonal, first lower-diagonal, and first upper-diagonal of $\hat{\mathbf{R}}$, respectively). Since $\rho_{j,j}$ is real, c_0 does not include any information on the CFO. This information is embedded in all the other polynomial coefficients, c_m. In contrast, c_m for $m \neq 0$ can be interpreted as the sum of the correlation coefficients between two different segments in the observed data vector.

Since $2G-1$ is usually small (for $4 \le G \le 8$), the $2G-1$ roots $\{\alpha_m\}_{m=1}^{2G-1}$ of the polynomial can be found with efficient root-finding algorithms [30]. We are interested in the root which is closest to one, denoted by α_1. Given this root, the estimated CFO is,

$$\hat{\epsilon} = -\frac{G}{2\pi}\arg(\alpha_1)\,. \tag{20}$$

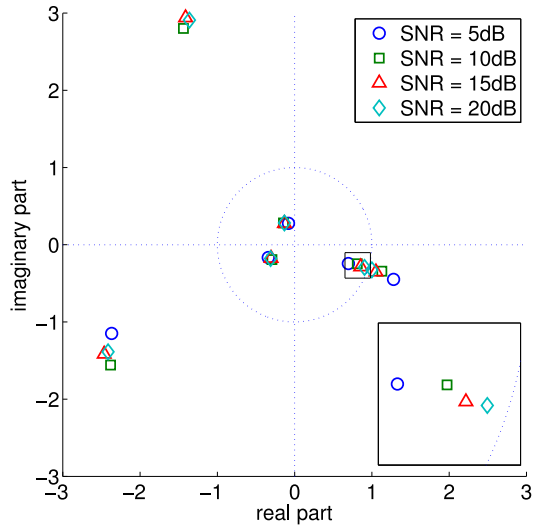

Fig. 2. An example of the roots of (19) for different values of SNR. The zoom is on the location of the root α_1.

We note that a rigorous proof on the uniqueness of this estimate is not provided and it may be argued that in some way it is an heuristic approach. However, the roots are based on the covariance matrix $\hat{\mathbf{R}}$. We showed in Appendix E that the rank of this $G \times G$ covariance matrix assuming sufficiently low noise level is $G-1$ with probability one. This means that there is only a single root for the solution of the cost function, and this one can be interpreted, at least under the small errors regime, as the root which is closest to zero.

Such an approach is similar to the Root-MUSIC method in array processing [31] where instead of performing a grid search in the direction of arrival space, a root in the z-plane is first determined and then the source direction is determined from the root phase. Further, the argument of α_1 is based on considering all possible correlations between different segments of the data as previously explained.

In Fig. 2 we demonstrate possible locations of the roots versus several values of SNR (see definition of the SNR and the details of the parameters of this example in Section IX.). It can be seen that the root α_1 changes its position only slightly as the SNR level decreases, which implies that such an estimate can be considered to be robust to noise. This conclusion is also corroborated in the simulation results.

VI. EVD-Based CFO Estimator

Another possible approach to determine the CFO based on the cost function in (16) is by performing a two-step approach, using the eigenvalue decomposition (EVD) technique. We express the matrix $\mathbf{Y}$ which appears in (17) as

$$\mathbf{Y}(L+1:Q,:) = \mathbf{Y}_0 + \mathrm{N}\,, \tag{21}$$

where $\mathbf{Y}_0$ is a $(Q-L)\times G$ matrix obtained from the noiseless observation vector $\mathbf{y}_0$ as

$$\mathbf{Y}_0 = [[\mathbf{R}_{\text{ola}}\mathbf{y}_0](L+1:Q), \cdots, [\mathbf{R}_{\text{ola}}\mathbf{y}_0](K-Q+L+1:K)], \tag{22}$$

and the $(Q-L)\times G$ matrix N is similarly defined as (22), where instead of $\mathbf{y}_0$ we use the measurement noise vector $\mathbf{n}$. Substituting (21) into (17) yields

$$\hat{\mathbf{R}} = \underbrace{\frac{1}{Q-L}\mathbf{Y}_0^H\mathbf{Y}_0}_{\triangleq \mathbf{R}_0} + \frac{1}{Q-L}(\mathrm{N}^H\mathbf{Y}_0 + \mathbf{Y}_0^H\mathrm{N} + \mathrm{N}^H\mathrm{N})\,. \tag{23}$$

Using the statistical distribution of the noise, which we assume it is a white noise sequence with variance equals to σ_n^2, the (k,m)th element of the second and third terms in (23) are approximately zero (each entry of theses matrices is related to the mean of the noise which is zero), while the (k,m)th element of the forth term in (23) is approximately zero for $k \neq m$ (since we assume a white noise sequence), and equals σ_n^2 for $n=m$. We thus obtain that approximately the matrix $\hat{\mathbf{R}}$ is given as,

$$\hat{\mathbf{R}} \;\cong\; \mathbf{R} = \mathbf{R}_0 + \sigma_n^2\mathbf{I}_G\,. \tag{24}$$

Notice that using $\mathbf{R}_0$ in place of $\hat{\mathbf{R}}$ in (16) yields that $\ell_1(\epsilon)=0$ for $\boldsymbol{\alpha}=\boldsymbol{\alpha}(\epsilon_0)$. This means that $\boldsymbol{\alpha}(\epsilon_0)$ is an eigenvector of $\mathbf{R}_0$ corresponding to the zero eigenvalue. In fact, the rank of $\mathbf{R}_0$ is $G-1$ with probability one (see the proof in Appendix E), that is, $\mathbf{R}_0$ has a single zero eigenvalue, and in turn, there is only a single CFO that solves (15). Further, recall that if $\mathbf{u}$ is an eigenvalue of a matrix $\mathbf{A}$ with a corresponding eigenvalue λ, i.e., $\mathbf{A}\mathbf{u}=\lambda\mathbf{u}$, then given a constant η^2 we have that $(\mathbf{A}+\eta^2\mathbf{I})\mathbf{u} = \lambda\mathbf{u}+\eta^2\mathbf{u} = (\lambda+\eta^2)\mathbf{u}$. Hence it follows that $\mathbf{u}$ is also an eigenvector of the matrix $\mathbf{A}+\eta^2\mathbf{I}$ with a corresponding eigenvalue equals to $\lambda+\eta^2$. Therefore, we conclude that the minimal eigenvalue of $\mathbf{R}$ and its associated eigenvector are,

$$\lambda_{\min}(\mathbf{R}) = \sigma_n^2\;, \mathbf{u}_{\min}(\mathbf{R}) = \mathbf{u}_{\min}(\mathbf{R}_0) = \alpha(\epsilon_0)\,. \tag{25}$$

We note that $\lambda_{\min}(\mathbf{R})$ is also the minimal value of (15) in this case. Based on (25) we conclude that approximately

$$\lambda_{\min}(\hat{\mathbf{R}}) \cong \lambda_{\min}(\mathbf{R})\;, \mathbf{u}_{\min}(\hat{\mathbf{R}}) \cong \mathbf{u}_{\min}(\mathbf{R})\,. \tag{26}$$

Note that as we are interested only in the smallest eigenvector of $\hat{\mathbf{R}}$, it can be determined using an efficient computation method such as the inverse iteration method [32] instead of performing a full eigenvalue decomposition.

We can now proceed to present the suggested method. Given the eigenvector $\mathbf{u}_{\min}(\hat{\mathbf{R}})$, we assume that it is slightly deviated as

$$\mathbf{u}_{\min}(\hat{\mathbf{R}}) \cong \mathbf{u}_{\min}(\mathbf{R}_0) + \delta\mathbf{u}_{\min}\,, \tag{27}$$

where $\delta\mathbf{u}_{\min}$ is a small perturbation with zero mean. We can further express the gth element of $\mathbf{u}_{\min}(\hat{\mathbf{R}})$ as

$$[\mathbf{u}_{\min}(\hat{\mathbf{R}})]_g = |[\mathbf{u}_{\min}(\hat{\mathbf{R}})]_g| e^{j\arg([\mathbf{u}_{\min}(\hat{\mathbf{R}})]_g)}\,. \tag{28}$$

Under this small errors assumption, i.e., $|[\delta\mathbf{u}_{\min}]_g| \ll |[\mathbf{u}_{\min}(\mathbf{R}_0)]_g| = 1/\sqrt{G}, g=0,\ldots,G-1$, it can be shown that the first order Taylor series approximation of the magnitude and phase in (28) are approximately (similar approximations are used for the parameter estimation of polynomial phase

signals [33]–[35])

$$\begin{aligned}
|[\mathbf{u}_{\min}(\hat{\mathbf{R}})]_g| &= |\Re\{[\mathbf{u}_{\min}(\mathbf{R}_0)]_g\} + \Re\{[\delta\mathbf{u}_{\min}]_g\} \\
&\quad + j(\Im\{[\mathbf{u}_{\min}(\mathbf{R}_0)]_g\} + \Im\{[\delta\mathbf{u}_{\min}]_g\})| \,, \\
&\cong |[\mathbf{u}_{\min}(\mathbf{R}_0)]_g| = \frac{1}{\sqrt{G}} \,, \\
\arg([\mathbf{u}_{\min}(\hat{\mathbf{R}})]_g) &= \tan^{-1}\Big(\frac{\Im\{[\mathbf{u}_{\min}(\mathbf{R}_0)]_g\} + \Im\{[\delta\mathbf{u}_{\min}]_g\}}{\Re\{[\mathbf{u}_{\min}(\mathbf{R}_0)]_g\} + \Re\{[\delta\mathbf{u}_{\min}]_g\}}\Big) \,, \\
&\cong \arg([\mathbf{u}_{\min}(\mathbf{R}_0)]_g) \\
&\quad - \frac{\Re\{[\delta\mathbf{u}_{\min}]_g \Im\{[\mathbf{u}_{\min}(\mathbf{R}_0)]_g\}\}}{|[\mathbf{u}_{\min}(\mathbf{R}_0)]_g|^2} \\
&\quad + \frac{\Im\{[\delta\mathbf{u}_{\min}]_g \Re\{[\mathbf{u}_{\min}(\mathbf{R}_0)]_g\}\}}{|[\mathbf{u}_{\min}(\mathbf{R}_0)]_g|^2} \,, \\
&\cong \arg([\mathbf{u}_{\min}(\mathbf{R}_0)]_g) \\
&\quad + G\Im\{[\delta\mathbf{u}_{\min}]_g ([\mathbf{u}_{\min}(\mathbf{R}_0)]_g)^*\} \,, \qquad (29)
\end{aligned}$$

where $\Re\{x\}$ and $\Im\{x\}$ are the real and imaginary parts of x, and also in the last transition we substituted $|[\mathbf{u}_{\min}(\mathbf{R}_0)]_g|^2 = G$. We note that though the current analysis approach is used, there are other approaches to analyze the perturbation of the eigenvector including the analysis given in [36]. The information on the CFO is hidden in the phases $\{\arg([\mathbf{u}_{\min}(\hat{\mathbf{R}})]_g)\}_{g=0}^{G-1}$. We assume that the phase noises are small enough that they do not cause any π jumps and a phase unwrapping process is not needed. We thus obtain the linear model for the CFO,

$$\arg([\hat{\mathbf{u}}_{\min}(\hat{\mathbf{R}})]_g) \cong -\frac{2\pi}{G} g\epsilon_0 + G\Im\{\underbrace{[\delta\mathbf{u}_{\min}]_g ([\mathbf{u}_{\min}(\mathbf{R}_0)]_g)^*}_{\triangleq \mu_g}\} \,. \qquad (30)$$

By collecting all the measurements in (30) into a vector-form model we obtain

$$\begin{bmatrix} \arg([\hat{\mathbf{u}}_{\min}(\hat{\mathbf{R}})]_0) \\ \vdots \\ \arg([\hat{\mathbf{u}}_{\min}(\hat{\mathbf{R}})]_{G-1}) \end{bmatrix} = -\frac{2\pi}{G} \begin{bmatrix} 0 \\ \vdots \\ G-1 \end{bmatrix} \epsilon_0 + \begin{bmatrix} \mu_0 \\ \vdots \\ \mu_{G-1} \end{bmatrix} . \qquad (31)$$

According to the LS estimation approach we select the CFO that minimizes the quadratic cost function

$$V(\epsilon) = \sum_{g=0}^{G-1} (\arg([\hat{\mathbf{u}}_{\min}(\hat{\mathbf{R}})]_g) + \frac{2\pi}{G} g\epsilon)^2 \,. \qquad (32)$$

After taking the derivative of (32) w.r.t. ϵ and equating the result to zero, we obtained the LS estimate of the CFO given as

$$\begin{aligned}
\hat{\epsilon} &= \frac{G}{2\pi} \frac{\sum_{g=0}^{G-1} \arg([\hat{\mathbf{u}}_{\min}(\hat{\mathbf{R}})]_g}{\sum_{g=0}^{G-1} g^2} \,, \\
&= -\frac{3}{\pi(G-1)(2G-1)} \sum_{g=0}^{G-1} g \cdot \arg([\hat{\mathbf{u}}_{\min}(\hat{\mathbf{R}})]_g) \,, \qquad (33)
\end{aligned}$$

which is a simple weighted sum of the arguments of an eigenvector. In the second transition in (33) we used the result $\sum_{g=0}^{G-1} g^2 = G(2G-1)(G-1)/6$. The mean and variance of the estimate in (33) are detailed in Appendix D.

VII. Computational Load

We evaluate the computational complexity of each method discussed by calculating the number of online real multiplications involved.

Consider first the cost function of the NLS-based method given in (13) which involves a grid search over a pre-defined interval of the CFO. Assuming that there are M hypothesized CFO values, the resolution of the grid needs to be small enough so that the required accuracy is reached. In Appendix B we show that the standard deviation CFO estimate reduces inversely with $\sqrt{K}$, and hence the number of points M needs to increase linearly with $\sqrt{K}$. For each hypothesized CFO value, the product $\mathbf{Y}\alpha(\epsilon)$ requires $\mathcal{O}((Q-L)G)$ multiplications, and taking the norm of this product requires $\mathcal{O}(G)$ further multiplications. Hence, in total, for M points in the grid, the complexity of the NLS-based method in (16) is $\mathcal{O}(M((Q-L)G+G))$ multiplications, and since $M \propto \sqrt{K}$ this complexity is approximately $\mathcal{O}(\sqrt{K}G(Q-L))$ multiplications.

The root-based method requires the computation of $\hat{\mathbf{R}}$ in (17) which carries $\mathcal{O}((Q-L)G^2)$ multiplications. This method further requires computing the polynomial coefficients, which is of complexity $\mathcal{O}(G^2)$, and finding the roots of a $2G-1$ order polynomial, which is of complexity $\mathcal{O}(G^3)$. The total complexity of this method assuming that $Q-L \gg G$ is $\mathcal{O}(G^2(Q-L))$.

Finally, the EVD-based method requires the computation of $\hat{\mathbf{R}}$ in (16) which again is of complexity $\mathcal{O}((Q-L)G^2)$ multiplications. The EVD-based method also requires $\mathcal{O}(G^3)$ multiplications for computing the smallest eigenvalue of $\mathbf{R}$. The total complexity of this method assuming that $Q-L \gg G$ is $\mathcal{O}(G^2(Q-L))$, as the complexity of the root-based method.

While the complexity of the NLS-based method increases w.r.t. $\sqrt{K}G$, that is, it depends on the number of carriers, the complexities of the proposed root-based and EVD-based methods increase w.r.t G^2. Since in practice G is usually small, this is a significant reduction of the computation load especially for power-limited and processing-limited underwater OFDM systems.

VIII. Peak to Average Power Ratio

One of the sensitive issues (at least from a practical point of view) of OFDM signaling is the PAPR. In this section we examine the PAPR of the proposed transmitted OFDM block. The nth sample of the discrete-time transmitted signal $\mathbf{F}_K^H \mathbf{s}$ (before zero-padding) is

$$\begin{aligned}
\tilde{s}(n) &= \sum_{q=0}^{Q-1} \frac{1}{\sqrt{K}} \underbrace{s(qG)}_{=u} e^{j\frac{2\pi}{Q}nq} + \underbrace{\sum_{k\in\mathcal{S}_D} \frac{1}{\sqrt{K}} s(k) e^{j\frac{2\pi}{K}nk}}_{\triangleq \eta(n)} \,, \\
&= \frac{Qu}{\sqrt{K}} \delta[n \bmod Q] + \eta(n) \,, n = 0, 1, \ldots, K-1 \,, \qquad (34)
\end{aligned}$$

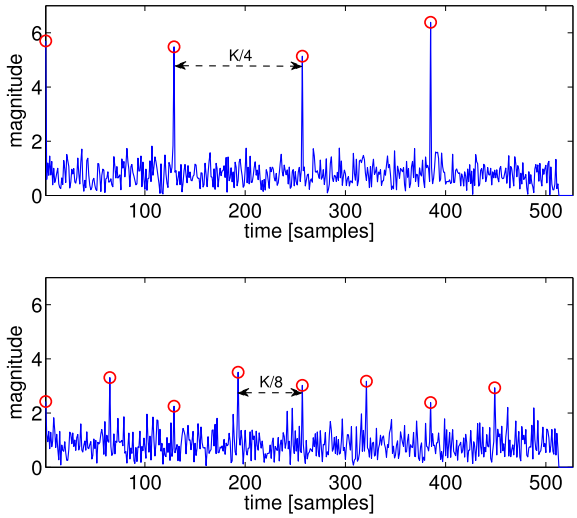

Fig. 3. Examples of the discrete time OFDM block ($G = 4$ for the upper plot, and $G = 8$ for the bottom plot).

TABLE I
PAPR [dB] FOR RANDOM AND IDENTICAL PILOT SELECTION

G	8	16	32
$\text{PAPR}_{\text{random}}$	8.4	8.4	8.4
$\text{PAPR}_{\text{identical}}$	12	9.1	8.6

where $\mathcal{S}_D$ is the set of indices of the data symbols, $\delta[\cdot]$ is the delta function, and in the second transition we used (14). We see that there are G peaks with absolute values equal to $Q/\sqrt{K}$ at times $n = 0, Q, \ldots, K - Q$ in the presence of a noise-like term $\eta(n)$. For $K \gg Q$ this noise term is distributed as a zero mean Gaussian random variable with variance equal to $(K - Q)/K$. The PAPR of the signal is given by

$$\text{PAPR} = \frac{\max|\tilde{s}(n)|^2}{\frac{1}{K}\sum_{n=1}^{K}|\tilde{s}(n)|^2} \cong \left(\frac{Q}{\sqrt{K}} + \sqrt{\frac{K-Q}{K}}\right)^2, \quad (35)$$

where the denominator of (35) equals one, and in the numerator of (35) we used the fact that the at every Q sample we obtain the coherent sum of the identical pilots, which their sum is $Q/\sqrt{K}$ in the presence of noise-like samples with standard deviation of $\sqrt{(K-Q)/K}$ which equals unity for $K \gg Q$.

In Fig. 3 we show two transmitted signals for $G = 4$ (upper plot) and for $G = 8$ (lower plot). In Table I we present the PAPR for random selection of pilots and for identical pilots versus G with $K = 512$ QPSK symbols. Notice that as G increases, the PAPR for identical pilot selection is similar to the random selection case. Still, even for smaller values of G, e.g., $G = 8$, we obtain a reasonable value of PAPR around 10 dB.

IX. Simulation Examples

We present simulation results that illustrate the performance of the discussed methods. The number of QPSK symbols is $K = 2048$ with bandwidth of $W = K\Delta f = 12.5$ KHz, which corresponds to a sampling interval $T_s = T/K = 1/W$ and $T = K/W$ is the block duration. The pilot frequency spacing is $G = 8$ pilot symbols. We simulated two underwater channels: a single path channel (also referred to as an impulse channel) and a multipath shallow-water acoustic channel using the statistical model in [28]. We considered a transmitter and a receiver at a depth of 5 meters, and the distance between them is 500 meters. The length of the acoustic channel (in samples) is approximately $L = 100$ which corresponds to a channel delay spread of 8 msec. As each of the K symbols is encoded with two bits, we define the bit energy as $E_b = E_s/(2K)$ where $E_s = T_s\|\mathbf{s}\|^2$ is the signal energy. We added a complex white Gaussian noise with variance $\sigma^2 = N_0 W/2$ where N_0 is the spectral density of the noise. We define the signal to noise ratio as SNR $= E_b/N_0$. The normalized CFO is fixed to $\epsilon_0 = 0.2$.

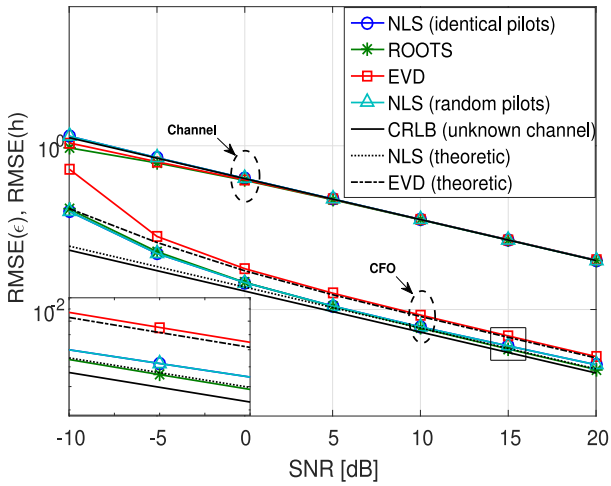

Fig. 4. RMSE of the channel ($\mathbf{h}$) and CFO (ϵ) estimates versus the SNR of the different estimation techniques.

In the first example we evaluate the RMSE of the CIR and the CFO estimates of each of the methods versus SNR, where for a given SNR we defined the RMSE as: $\text{RMSE}(\mathbf{h}) = \sqrt{\frac{1}{N_{\text{exp}}}\sum_{i=1}^{N_{\text{exp}}}\|\mathbf{h} - \hat{\mathbf{h}}_i\|^2}$ and $\text{RMSE}(\epsilon) = \sqrt{\frac{1}{N_{\text{exp}}}\sum_{i=1}^{N_{\text{exp}}}(\epsilon_0 - \hat{\epsilon}_i)^2}$, and $\hat{\mathbf{h}}_i$ and $\hat{\epsilon}_i$ are the CIR and CFO estimates at the ith trial, and the number of trials is $N_{\text{exp}} = 1000$. We varied the SNR from -10 dB to 20 dB with a step of 5 dB. For the NLS-based methods, for both random pilot selection (Section IV) and identical pilot selection (Section V), we used a grid range of normalized CFO of $[-0.7, 0.7]$ with a step of 0.005. The results are shown in Fig. 4. We also plot the CRLB assuming the channel is unknown, and the theoretical variance of the CFO estimates using (71). The plotted CRLB is obtained by computing the CRLB on the CFO as detailed in Appendix B, and then taking its square root. Specifically, we note that the CFO ϵ is derived under the assumption that the channel $\mathbf{h}$ is unknown. Therefore, we derive the Fisher information matrix for all the unknowns (ϵ, and $\mathbf{h}$) as detailed in Appendix B, and then compute the CRLB on the CFO as expressed in eq. (48) in Appendix B. This CRLB on the CFO takes into account the fact the channel is not known to the receiver. If the channel was known, then the CRLB was smaller. This is the meaning of the labeling associated with the CRLB in Fig. 4. As can be seen all methods are close to the CRLB at a sufficiently high SNR. The root-based (Section V) and the EVD-based (Section VI) methods have similar RMSE as the NLS-based method for medium

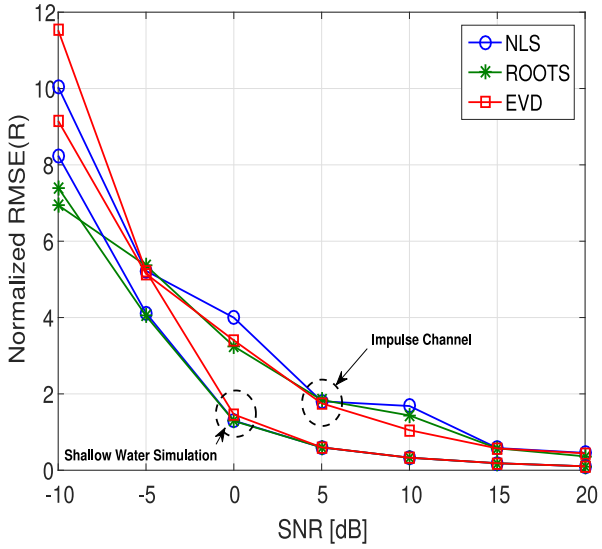

Fig. 5. Communication performance in terms of normalized RMSE(R) vs. SNR.

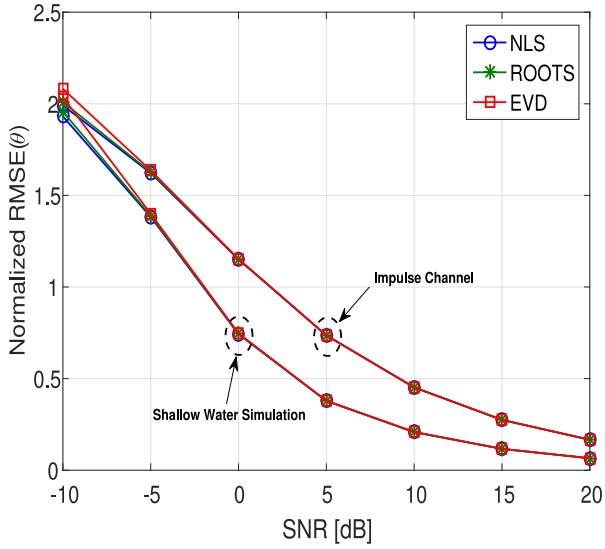

Fig. 6. Communication performance in terms of normalized RMSE(θ) vs. SNR.

to high SNR. The theoretical variance of the normalized CFO is close to the CRLB for almost all values. Also, the error of the NLS-based method for random pilots is similar to that of the NLS-based method with identical pilots, and thus in the sequel we only focus on the performance of the latter.

In the second example we illustrate the mean square error in decoding the data symbols. Using the same setup as detailed in the first example, we proceed to decode the QPSK transmitted data symbols. For a given SNR, we define the normalized RMSE of the symbol constellation both in Euclidean distance and phase as $\text{RMSE}(R) = \frac{1}{1/\sqrt{2}}\sqrt{\frac{1}{N_{\text{exp}}}\sum_{i=1}^{N_{\text{exp}}}\sum_{k\in\mathcal{S}_D}|s_i(k)-\hat{s}_i(k)|^2}$ and $\text{RMSE}(\theta) = \frac{1}{\pi/4}\sqrt{\frac{1}{N_{\text{exp}}}\sum_{i=1}^{N_{\text{exp}}}\sum_{k\in\mathcal{S}_D}|\arg(s_i(k))-\arg(\hat{s}_i(k))|^2}$ where $\hat{s}_i(k)$ is the k decoded data symbol at the ith trial. In Figs. 5 and 6 we show RMSE(R) and RMSE(θ) respectively for an impulse channel and the simulated shallow water channel. As expected the impulse channel results in better performance in both cases. In consistency with the CFO and CIR simulation results, we see that for high SNR (above 0 dB in these simulations) the performance of all three methods are similar. Simulations for $K = 512$ OFDM blocks produced similar results, and therefore are not presented here.

X. Real-Data Results

We examined the proposed methods in pool tank experiments and sea trials.

A. Pool Trial Results

The pool experiments were conducted in a $10\,\text{m} \times 20\,\text{m} \times 10\,\text{m}$ acoustic tank. The receiving and transmitting acoustic transducers were placed at the center of the pool 2 m apart at 3 m depth. Since the typical CIR in the tank is fairly long, we used $K = 2048$ and $G = 4$, which results in a channel length (in samples) of $L = 250$. A total of 60 OFDM packets were

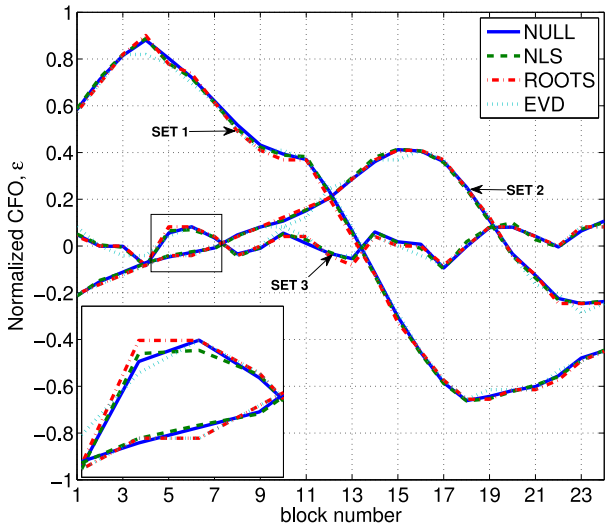

Fig. 7. CFO estimates of three motion sets in the pool trial.

transmitted during the trial, including both static and in-motion scenarios. For the latter, in order to produce minor motions, the transmitting hydrophone was manually displaced to create a pendulum-like motion. Fig. 7 shows the CFO for of three sets of motion scenarios. In each set a different displacement was performed, e.g., in set 1, the transmitter displacement was $x_d = 20$ cm. Using the CFO estimates we can assume that the motion was approximately harmonic, with a period of $T_p \cong 4.5$ sec (since 24 blocks are transmitted in 4.3 seconds and the hydrophone nearly completed a cycle in that time) and the estimated velocity amplitude and displacement are

$$v_{\max} = \frac{c\Delta f \epsilon_{\max}}{f_c} \cong 0.3\,\text{m/sec} \longrightarrow \frac{v_{\max} T_p}{2\pi} = 21\,\text{cm} \cong x_d\,, \tag{36}$$

where according to Fig. 7, $\epsilon_{\max} \cong 0.8$ is the maximum normalized CFO estimated in the packet. As can be seen, all three

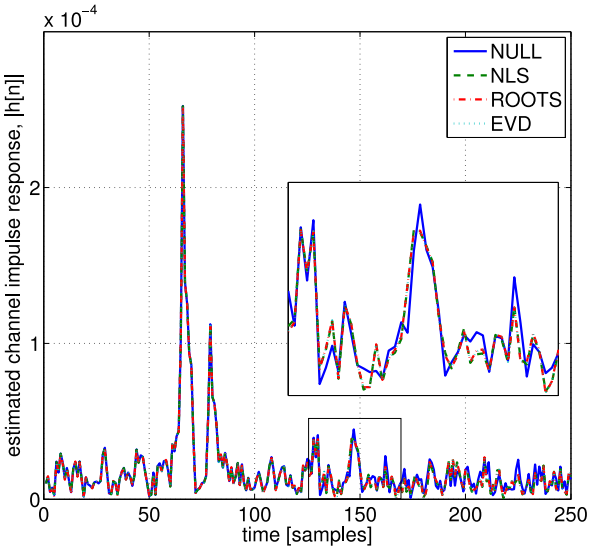

Fig. 8. An example of the estimated CIR response in the pool trial.

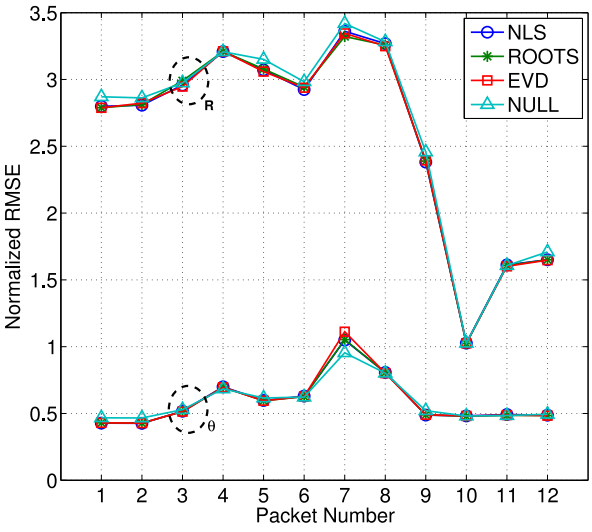

Fig. 9. Pool trial decoded data RMSE results.

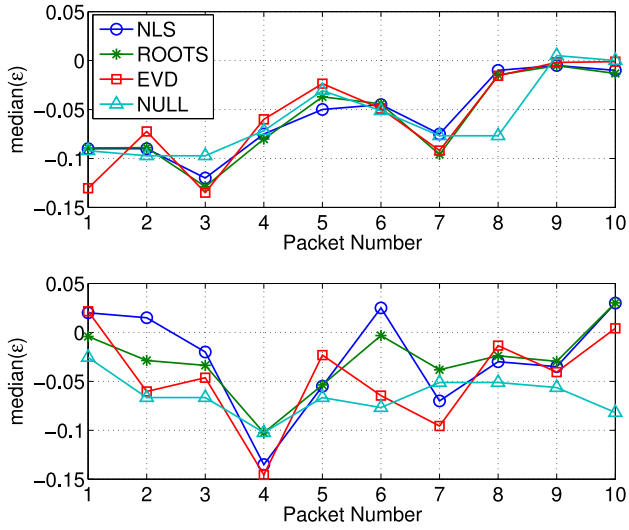

Fig. 10. Sea trial CFO estimates. Results for receiver 1 (located 400 m from the transmitter) are plotted in the upper plot. The results of Receiver 2 (100 m) are plotted at the bottom plot.

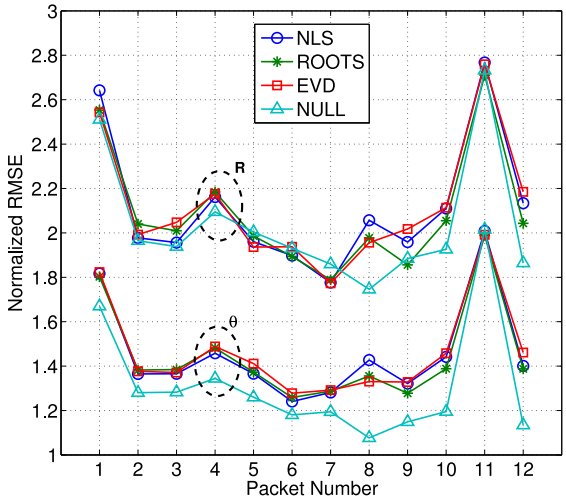

Fig. 11. The sea trial decoded data rmse results.

methods agree and produce similar estimates compared to the state of the art null-carriers CFO estimate [8] (the search grid and step size of the null and NLS methods were identical and were performed as detailed in the numerical simulations part). The CIR estimated with all four methods (including the null-estimation) were also consistent, as can be seen in the example shown in Fig. 8. The estimated channel has a strong direct path, followed by the surface reflection (around sample 80), tank side reflection (sample 130) and tank floor reflection (sample 145). As could be expected, following the CFO and CIR estimates, the communication performance was similar for all methods. Fig. 9 shows both the Euclidean and phase RMSEs for 12 packets transmitted during the pool trial. As mentioned, a unit RMSE corresponds to $\pi/4$ phase error and $1/\sqrt{2}$ Euclidean error. As can be seen, there is no error in the phase of the symbols and thus the decoded data is almost error free. In the second part of the trial the receiver-transmitter distance was reduced from 2.5 m to 2 m. Packets 9–12 are taken from this last part, which caused the Euclidean RMSE to drop.

B. Sea Trial Results

The second trial was conducted in Haifa port in Israel. Two widely separated receivers were placed near the harbor docks 400 m and 100 m from a single transmitter placed on a tugboat. In this trial we used $K = 512$ and $G = 4$. Due to significant shipping activity in the harbor, the received signals contained non-white noise and transient noises which affected the receivers performance. Fig. 10 shows the median of the CFO estimate obtained from ten OFDM packets received at the two receivers (a median filter was used to mitigate the effect of outliers estimates due to transient noises). Compared to the numerical simulations and pool experiments, the estimation errors in the sea trial are less consistent between all methods. However, looking

at Fig. 11, we can see that this does not have significant effect on the communications RMSE performance. The RMSE is computed by taking packets from both receivers. The SNR of these packets varied between -3 dB and 2 dB. For these kind of SNR values the simulated shallow water RMSEs were similar (see Figs. 5 and 6).

XI. Conclusion

We proposed low-complexity methods for estimating the residual Doppler shift for underwater acoustic multicarrier transmissions by finding the roots of a small order polynomial or using a least squares estimate given the phases of the minimal eigenvector of a small data matrix. Each of these methods involves computational complexity reduction on the order of a magnitude w.r.t. the state of the art CFO estimation methods for UAC OFDM communication. Simulations show that the proposed methods have similar mean square error performance as the common exhaustive-based methods and are close to the associated Cramer-Rao lower bound, and also result in small mean square symbol detection errors. Pool experiments and sea trials further emphasized these performance results. These results are important for practical UAC systems with limited processing resources.

Appendix A
Derivation of $\mathbf{x}(\epsilon)$

In this appendix we derive the expression for $\mathbf{x}(\varepsilon)$ in (7). Consider the $Q \times K$ matrix $\mathbf{T}_{sc}\mathbf{F}_K$ which its qth row is,

$$[\mathbf{T}_{sc}\mathbf{F}_K]_q = \frac{1}{\sqrt{K}} e^{-j\frac{2\pi}{Q}kq}\,, \begin{array}{l} q=0,\ldots,Q-1 \\ k=0,\ldots,K-1 \end{array}, \tag{37}$$

which means that $\mathbf{T}_{sc}\mathbf{F}_K$ is expressed in a matrix form as,

$$\mathbf{T}_{sc}\mathbf{F}_K = \frac{1}{\sqrt{G}}[\,\mathbf{F}_Q\big|\cdots\big|\mathbf{F}_Q\,], \tag{38}$$

where $\mathbf{F}_Q$ is a $Q \times Q$ matrix with the (m,n)th element given by $\frac{1}{\sqrt{Q}} e^{-j\frac{2\pi}{Q}\cdot mn}$. Next consider the matrix $\mathbf{R}_{\text{ola}}\mathbf{\Gamma}_K^H(\epsilon)\mathbf{y}$. Using simple algebraic steps we can express it as

$$\mathbf{R}_{\text{ola}}\mathbf{\Gamma}_K^H(\epsilon)\mathbf{y} = \begin{bmatrix} \mathbf{\Gamma}_K^H(1:L)\mathbf{y}(1:L) \\ \quad +\mathbf{\Gamma}_K^H(K:P)\mathbf{y}(K+1:P) \\ \mathbf{\Gamma}_K^H(L+1:Q)\mathbf{y}(L+1:Q) \\ \vdots \\ \mathbf{\Gamma}_K^H(K-Q+1:K-Q+L) \\ \quad \times\mathbf{y}(K-Q+1:K-Q+L+1) \\ \mathbf{\Gamma}_K^H(K-Q+L+1:K) \\ \quad \times\mathbf{y}(K-Q+L+1:K) \end{bmatrix}, \tag{39}$$

where for notation simplicity $\mathbf{\Gamma}_K(n:m)$ stands for the submatrix $\mathbf{\Gamma}_K(n:m, n:m)$. Observe that for $g = 0,\ldots,G-1$

$$\mathbf{\Gamma}_K(gQ+u:gQ+v) = \mathbf{\Gamma}_Q(u:v)e^{j\frac{2\pi}{G}g\epsilon}\,, u \le v \in \{1,\ldots,Q\}\,, \tag{40}$$

Also note that $\mathbf{\Gamma}_K(K:P) = \mathbf{\Gamma}_K(QG:QG+L) = \mathbf{\Gamma}_Q(1:L)$. Hence we obtain that (41) can be further expressed as

$$\mathbf{R}_{\text{ola}}\mathbf{\Gamma}_K^H(\epsilon)\mathbf{y} = \begin{bmatrix} \mathbf{\Gamma}_Q^H(1:L)(\mathbf{y}(1:L)+\mathbf{y}(K+1:P)) \\ \mathbf{\Gamma}_Q^H(L+1:Q)\mathbf{y}(L+1:Q) \\ \vdots \\ e^{-j\frac{2\pi}{G}(G-2)\epsilon}\mathbf{\Gamma}_Q^H(1:L) \\ \quad \times\mathbf{y}(K-Q+1:K-Q+L+1) \\ e^{-j\frac{2\pi}{G}(G-1)\epsilon}\mathbf{\Gamma}_Q^H(L+1:Q) \\ \quad \times\mathbf{y}(K-Q+L+1:K) \end{bmatrix}, \tag{41}$$

By multiplying (38) by (41) we obtain $\mathbf{x}(\epsilon)$ in (7). This concludes the derivation.

Appendix B
The Cramer-Rao Lower Bound

In this appendix we derive the CRLB on the unknown parameters of the model. The CRLB provides lower bound on the covariance of any unbiased estimator of the parameter vector given the $P \times 1$ measurement vector $\mathbf{y}$ in (4). The measurement vector $\mathbf{y}$ is distributed as $\mathbf{y} \sim \mathcal{NC}(\mu(\theta), \sigma_n^2\mathbf{I}_P)$ where $\mu(\theta) = \mathbf{\Gamma}_K(\epsilon_0)\mathbf{H}\mathbf{T}_{zp}\mathbf{F}_K^H\mathbf{s}$ and θ is a $2(K-Q+L)\times 1$ vector of unknown parameters of the model given as

$$\theta \triangleq [\epsilon_0, \mathbf{h}_r^T, \mathbf{h}_i^T, \mathbf{s}_{d,r}^T, \mathbf{s}_{i,r}^T]^T\,, \tag{42}$$

where $\mathbf{h}_r$ and $\mathbf{h}_i$ are the real and imaginary parts of the channel impulse response $\mathbf{h}$, and $\mathbf{s}_{d,r}$, $\mathbf{s}_{d,i}$ are the real and imaginary parts of the vector containing the data symbols only.

The CRLB is obtained by taking the inverse of the $(2(K-Q+L))\times(2(K-Q+L))$ Fisher information matrix (FIM) which its (m,n)th element is given as [31]

$$[\mathbf{F}(\theta)]_{m,n} = \frac{2}{\sigma_n^2}\Re\{(\frac{\partial\boldsymbol{\mu}(\theta)^H}{\partial\theta_n})^H\frac{\partial\boldsymbol{\mu}(\theta)}{\partial\theta_m}\}\,. \tag{43}$$

The FIM associated with the CFO, for example, is given by $f_{\epsilon_0,\epsilon_0} = \frac{2}{\sigma_n^2}\Re\{(\partial\boldsymbol{\mu}(\theta)^H/\partial\epsilon)^H\partial\boldsymbol{\mu}(\theta)/\partial\epsilon\}$. Similarly we can define $\mathbf{f}_{\epsilon_0,\mathbf{h}} = [\mathbf{f}_{\epsilon_0,\mathbf{h}_r}\,|\,\mathbf{f}_{\epsilon_0,\mathbf{h}_i}]$ and $\mathbf{F}_{\mathbf{h},\mathbf{h}} = [\mathbf{F}_a\,|,\mathbf{F}_b]$ with $\mathbf{F}_a = [\mathbf{F}_{\mathbf{h}_r,\mathbf{h}_r}^T, \mathbf{F}_{\mathbf{h}_r,\mathbf{h}_i}^T]^T$ and $\mathbf{F}_b = [\mathbf{F}_{\mathbf{h}_r,\mathbf{h}_i}^T, \mathbf{F}_{\mathbf{h}_i,\mathbf{h}_i}^T]^T$. As can be seen all the FIMs depend on the partial derivatives of the mean $\mu(\theta)$ on the parameters of the model. These derivatives are given as

$$\frac{\partial\boldsymbol{\mu}(\theta)}{\partial\epsilon_0} = j\frac{2\pi}{K}\mathbf{U}\mathbf{y}_0\,, \tag{44}$$

$$\frac{\partial\boldsymbol{\mu}(\theta)}{\partial h_r(\ell)} = -j\frac{\partial\boldsymbol{\mu}(\theta)}{\partial h_i(\ell)} = \mathbf{\Gamma}_K(\epsilon_0)\tilde{\mathbf{I}}_\ell\mathbf{T}_{zp}\mathbf{F}_K^H\mathbf{s}\,, \tag{45}$$

$$\frac{\partial\boldsymbol{\mu}(\theta)}{\partial s_{d,r}(q)} = -j\frac{\partial\boldsymbol{\mu}(\theta)}{\partial s_{d,i}(q)} = \mathbf{\Gamma}_K(\epsilon_0)\mathbf{H}\mathbf{T}_{zp}\mathbf{F}_K^H\mathbf{e}_q\,, \tag{46}$$

where $\mathbf{U} = \text{diag}(0,1,\ldots,P-1)$ is a $P\times P$ matrix, $\tilde{\mathbf{I}}_\ell$ where $\ell = 0,1,\ldots,L$ is a $P\times K$ matrix with ones on the sub-diagonal with indices $\{(\ell+m,m)\}_{m=1}^L$ and all other elements equal zero, and $\mathbf{e}_q$ is a $K\times 1$ vector with one on the qth element (associated with the index of the qth data symbol) and all other elements equal to zero.

For example, assuming that the channel and data symbols were known at the receiver, the CRLB on estimating the CFO would be,

$$\text{var}(\epsilon_0) \geq f^{-1}_{\epsilon_0,\epsilon_0} = \frac{\sigma^2 K^2}{2(2\pi)^2}\frac{1}{\|\mathbf{U}\mathbf{y}_0\|^2} = \frac{\sigma^2}{8\pi^2\rho}\frac{K^2}{\sum_{k=0}^{K-1}k^2}\,, \tag{47}$$

where $\rho \stackrel{\Delta}{=} \sum_{k=0}^{K-1} k^2 y_0^2(k)/\sum_{k=0}^{K-1} k^2$. Notice that $\sum_{k=0}^{K-1} k^2 = (K-1)K(2K-1)/6$, and therefore, we see that since $K \gg 1$, the variance on the CFO reduces inversely w.r.t. K. Similarly, assuming that data symbols are known we obtain that the variance of any unbiased estimate of the CFO is lower bounded as

$$\text{var}(\epsilon_0) \geq (f_{\epsilon_0,\epsilon_0} - \mathbf{f}_{\epsilon_0,\mathbf{h}}\mathbf{F}^{-1}_{\mathbf{h},\mathbf{h}}\mathbf{f}^T_{\epsilon_0,\mathbf{h}})^{-1}\,. \tag{48}$$

This concludes the derivation.

Appendix C
Small Error Analysis of the NLS-Based Method

In this appendix we derive the mean and variance of the NLS-based CFO estimate in (15). The mean and variance of the CFO estimate which minimizes (16) assuming small errors are [27],

$$E\{\hat{\epsilon}\} \cong \epsilon_0 - \frac{E\{\ell_1^{(1)}\}}{E\{\ell_1^{(2)}(\epsilon_0)\}}\,, \tag{49}$$

$$\text{var}\{\hat{\epsilon}\} \cong \frac{E\{|\ell_1^{(1)}(\epsilon_0)|^2\}}{(E\{\ell_1^{(2)}(\epsilon_0)\})^2}\,, \tag{50}$$

where $\{\ell_1^{(i)}(\epsilon_0)\}_{i=1}^2$ is the ith derivative of $\ell_1(\epsilon)$ evaluated at $\epsilon = \epsilon_0$. The cost function in (16) is expressed as,

$$\ell_1(\epsilon) = \frac{1}{G(Q-L)}\sum_{q=L}^{Q-1}\left|\sum_{g=0}^{G-1} y^{(g)}(q)e^{-j\frac{2\pi}{G}g\epsilon_0}\right|^2\,, \tag{51}$$

where we define $y^{(g)}(q)$ as the qth element of the gth segment of the the vector $\mathbf{y}$. We note that $y^{(g)}(q) = y_0^{(g)}(q) + n^{(g)}(q)$, where $y_0^{(g)}(q)$ is the noise free value of $y^{(g)}(q)$, and $n^{(g)}(q)$ is the qth element of the gth segment of $\mathbf{n}$. We define the following parameters for $u = 0, 1, 2$,

$$\bar{y}_u(q) = \sum_{g=0}^{G-1} g^u y_0^{(g)}(q)e^{-j\frac{2\pi}{G}g\epsilon_0}\,, \tag{52}$$

$$\bar{n}_u(q) = \sum_{g=1}^{G-1} g^u n^{(g)}(q)e^{-j\frac{2\pi}{G}g\epsilon_0}\,. \tag{53}$$

Note that $E\{\bar{n}_u(q)\} = 0$. Also since for $g_1, g_2 \in \{0,\ldots,G-1\}$, and $q_1, q_2 \in \{L,\ldots,Q-1\}$ we have $E\{n^{(g_1)}(q_1)n^{(g_2)}(q_2)\} = 0$ and $E\{n^{(g_1)}(q_1)n^{(g_2)^*}(q_2)\} = \sigma^2\delta(g_1-g_2)\delta(q_1-q_2)$, where $\delta(k)$ is the delta of Kronecker, we get that $E\{\bar{n}_{u_1}(q_1)\bar{n}_{u_2}(q_2)\} = 0$ for $u_1, u_2 \in \{0,1,2\}$ while,

$$E\{\bar{n}_{u_1}(q_1)\bar{n}^*_{u_2}(q_2)\} = \sigma_n^2\sum_{g=0}^{G-1} g^{u_1+u_2}\delta(q_1-q_2)\,, \tag{54}$$

which means that $E\{\bar{n}_{u_1}(q_1)\bar{n}^*_{u_2}(q_2)\}$ equals (i) $G\sigma_n^2$ for $u_1 = 0, u_2 = 0$; (ii) $\frac{1}{2}(G-1)G\sigma_n^2$ for $u_1 = 0, u_2 = 1$ or $u_1 = 1, u_2 = 0$; (iii) $\frac{1}{6}(G-1)G(2G-1)\sigma_n^2$ for $u_1 = 0, u_2 = 2$, or $u_1 = 1, u_2 = 1$, or $u_1 = 2, u_2 = 0$.

The first and second derivatives of $\ell_1(\epsilon_0)$ are then given as,

$$\ell^{(i)}(\epsilon_0) = \ell_d^{(i)}(\epsilon_0) + \ell_r^{(1)}(\epsilon_0)\,, i = 1, 2\,, \tag{55}$$

where $\ell_d^{(i)}(\epsilon_0)$ and $\ell_r^{(i)}(\epsilon_0)$ are the deterministic and random parts of $\ell^{(i)}(\epsilon_0)$ for $i = 1, 2$ which are given as

$$\ell_d^{(1)}(\epsilon_0) = -\frac{4\pi}{G(Q-L)}\sum_{q=L}^{Q-1}\Im\{\bar{y}_0(q)\bar{y}_1^*(q)\}\,, \tag{56}$$

$$\begin{aligned}\ell_r^{(1)}(\epsilon_0) = &-\frac{4\pi}{G(Q-L)}\sum_{q=L}^{Q-1}\Im\{\bar{n}_0(q)\bar{y}_1^*[q]\\ &+\bar{y}_0[q]\bar{n}_1^*(q) + \bar{n}_0(q)\bar{n}_1^*(q)\}\,,\end{aligned} \tag{57}$$

$$\ell_d^{(2)}(\epsilon_0) = -\frac{8\pi^2}{G^2(Q-L)}\sum_{q=L}^{Q-1}\Re\{\bar{y}_0(q)\bar{y}_2^*(q)\} - |\bar{y}_1(q)|^2\,, \tag{58}$$

$$\begin{aligned}\ell_r^{(2)}(\epsilon_0) = &-\frac{8\pi^2}{G^2(Q-L)}\sum_{q=L}^{Q-1}\Re\{\bar{n}_0(q)\bar{y}_2(q)^* + \bar{y}_0(q)\bar{n}_2^*(q)\\ &-\bar{y}_1(q)\bar{n}_1^*(q) - \bar{n}_1(q)\bar{y}_1(q)^*\\ &+\bar{n}_0(q)\bar{n}_2^*[q] - \bar{n}_1(q)\bar{n}_1^*[q]\}\,.\end{aligned} \tag{59}$$

Observe that $\ell_d^{(1)}(\epsilon_0) = 0$ as it is the derivative of (16) at the true CFO without noise, and therefore $\ell_1^{(1)}(\epsilon_0) = \ell_r^{(1)}(\epsilon_0)$.

Since the $\text{E}\{\bar{n}_u(q)\} = 0$, $u = 0, 1, 2$, and by using (54) we obtain that the mean of the first and second derivatives are,

$$E\{\ell_1^{(1)}(\epsilon_0)\} = -2\pi(G-1)\sigma^2\,, \tag{60}$$

$$E\{\ell_1^{(2)}(\epsilon_0)\} = \ell_d^{(2)}(\epsilon)\,, \tag{61}$$

where in (61) we note that $\Re\{E\{\bar{n}_0(q)\bar{n}_2^*(q)\}\} = E\{|\bar{n}_1(q)|^2\}$. The square of the first derivative in (16) is (neglecting terms that contain products of more than two noise terms),

$$\begin{aligned}[\ell_1^{(1)}(\epsilon_0)]^2 \cong &\frac{16\pi^2}{G^2(Q-L)^2}\sum_{q_1,q_2=L}^{Q-1}\Im\{\bar{n}_0(q_1)\bar{y}_1^*(q_1)\}\\ &\times\Im\{\bar{n}_0(q_2)\bar{y}_1^*(q_2)\}\\ &+\Im\{\bar{y}_0(q_1)\bar{n}_1^*(q_1)\}\Im\{\bar{y}_0(q_2)\bar{n}_1^*(q_2)\}\\ &+2\Im\{\bar{n}_0(q_1)\bar{y}_1^*(q_1)\}\Im\{\bar{y}_0(q_2)\bar{n}_1^*(q_2)\})\,.\end{aligned} \tag{62}$$

Taking the expectation of (62) and noting that $\{\bar{n}_u(q)\}$ are independent and identical random variables w.r.t. to the time

index q yields,

$$\begin{aligned} E\{[\ell_1^{(1)}(\epsilon_0)]^2\} = & \frac{16\pi^2}{G^2(Q-L)^2}\Bigg(\sum_{q=L}^{Q-1}\frac{1}{2}|\bar{y}_0(q)|^2E\{|\bar{n}_1(q)|^2\} \\ & + \frac{1}{2}|\bar{y}_1(q)|^2E\{|\bar{n}_0(q)|^2\} \\ & - \sum_{q=L}^{Q-1}\Re\{\bar{y}_0(q)\bar{y}_1^*(q)E\{\bar{n}_0(q)\bar{n}_1^*(q)\}\}\Bigg), \\ \overset{\text{by (54)}}{=} & \frac{8\pi^2\sigma^2}{G(Q-L)^2}\sum_{q=L}^{Q-1}[|\bar{y}_1(q)|^2 \\ & -(G-1)\Re\{\bar{y}_0(q)\bar{y}_1^*(q)\}]. \end{aligned} \tag{63}$$

The first summation involving $|\bar{y}_0(q)|^2$ equals zero as it equals $\ell_d^{(1)}(\epsilon_0)$ up to a constant. Also, according to (61) we have,

$$(E\{\ell_1^{(2)}(\epsilon_0)\})^2 = (\ell_d^{(2)}(\epsilon_0))^2. \tag{64}$$

Finally, we can express (52) in a compact form as

$$\bar{y}_u(q) = (\mathbf{y}_0^{(q)})^T\mathbf{\Phi}_u\alpha(\epsilon_0), \tag{65}$$

where $\mathbf{y}_0^{(q)}$ is the gth segment of the noise-free vector $\mathbf{y}_0$ is the gth segment of the noise-free vector $\mathbf{y}_0$, and $\mathbf{\Phi}_u = \text{diag}(0^u, 1^u, \ldots, (G-1)^u)$. This means that

$$\frac{1}{Q-L}\sum_{q=L}^{Q-1}\bar{y}_{u_1}(q)\bar{y}_{u_2}^*(q) = \alpha(\epsilon_0)^T\mathbf{\Phi}_{u_1}\mathbf{R}_0\mathbf{\Phi}_{u_2}\alpha(\epsilon_0)^*, \tag{66}$$

where $\mathbf{R}_0$ is defined in (23). Using (66) it can then be shown that (63) and (64) are

$$\text{E}\{[\ell_1^{(1)}(\epsilon_0)]^2\} = \frac{8\pi^2\sigma^2}{G(Q-L)}(\gamma_{1,1} - (G-1)\gamma_{0,1}), \tag{67}$$

$$E\{\ell_1^{(2)}(\epsilon_0)\} = -\frac{8\pi^2}{G^2}(\gamma_{1,1} - \gamma_{1,2}), \tag{68}$$

where we define the scalar $\{\gamma_{u,u'}\}$ for $(u,u') \in \{0,1,2\}$ as,

$$\gamma_{u,u'} \triangleq \Re\{\alpha(\epsilon_0)^H\mathbf{\Phi}_u\mathbf{R}_0\mathbf{\Phi}_{u'}\alpha(\epsilon_0)\}. \tag{69}$$

Substituting these results in (49) and (50) we obtain that the mean and the variance are,

$$E\{\hat{\epsilon}\} \cong \epsilon_0 + \sigma^2\frac{G^2(G-1)}{4\pi(\gamma_{1,1}-\gamma_{1,2})}, \tag{70}$$

$$\text{var}(\hat{\epsilon}) \cong \sigma^2\frac{G^3}{8\pi^2(Q-L)}\frac{\gamma_{1,1}-(G-1)\Re\{\gamma_{0,1}\}}{(\gamma_{1,1}-\gamma_{1,2})^2}, \tag{71}$$

where we define the scalar $\{\gamma_{u,u'}\}$ for $(u,u') \in \{0,1,2\}$ as,

$$\gamma_{u,u'} \triangleq \Re\{\alpha(\epsilon_0)^H\mathbf{\Phi}_u\mathbf{R}_0\mathbf{\Phi}_{u'}\alpha(\epsilon_0)\}, \tag{72}$$

where $\mathbf{\Phi}_u = \text{diag}(0^u, 1^u, \ldots, (G-1)^u)$, and $\mathbf{R}_0$ is the noise-free matrix $\hat{\mathbf{R}}$ as defined in (23). We see that the variance of the estimated CFO is proportional to G^4/K, which means that the variance decreases inversely w.r.t. the number of carriers K as given by the CRLB. This concludes the derivation.

Appendix D
Small Error Analysis of the EVD-Based Method

In this appendix we derive the mean and variance of the EVD-based estimator in (33). The first term on the right side on (30) is the noise-free model while the the second term is the perturbation of the phase due to noise model. Substituting (30) into (33) yields,

$$\hat{\epsilon} \cong \epsilon_0 - \beta\sum_{g=0}^{G-1} g\,\Im\{\mu_g\}, \tag{73}$$

where we define the parameter $\beta = \frac{3}{\pi(G-1)(2G-1)}$. Since the mean of $[\delta\mathbf{u}_{\text{min}}]_g$ is zero it is obvious that the mean of μ_g is also zero, and thus $E\{\hat{\epsilon}\} = \epsilon_0$, which means that approximately the CFO estimate in (33) is unbiased. The variance of the CFO estimate is

$$\begin{aligned} \text{Var}\{\hat{\epsilon}\} = & \beta^2G^2\sum_{g,\tilde{g}=0}^{G-1} g\tilde{g}\,\text{E}\{\Im\{\mu_g\}\Im\{\mu_{\tilde{g}}\}\}, \\ = & \beta^2G^2\sum_{g,\tilde{g}=0}^{G-1} g\tilde{g}\,\text{E}\{\Im\{\mu_g\frac{1}{2j}(\mu_{\tilde{g}}-\mu_{\tilde{g}}^*)\}\}, \\ \overset{\text{by (30)}}{=} & \frac{\beta^2G^2}{2}\Re\{\boldsymbol{\alpha}^H(\epsilon_0)\mathbf{C}E\{\delta\mathbf{u}_{\text{min}}\delta\mathbf{u}_{\text{min}}^H\}\mathbf{C}\boldsymbol{\alpha}(\epsilon_0) \\ & - \boldsymbol{\alpha}^H(\epsilon_0)\mathbf{C}E\{\delta\mathbf{u}_{\text{min}}\delta\mathbf{u}_{\text{min}}^T\}\mathbf{C}\boldsymbol{\alpha}^*(\epsilon_0)\}, \end{aligned} \tag{74}$$

where in the third transition in (74) we used the property that for complex scalar x, $\Im\{jx\} = \Re\{x\}$. Also, we define the $G \times G$ matrix $\mathbf{C} = \text{diag}(0, 1, \ldots, G-1)$ and under the presence of small errors [29],

$$\begin{aligned} E\{\delta\mathbf{u}_{\text{min}}\delta\mathbf{u}_{\text{min}}^H\} = & \mathbf{\Omega} + \frac{\sqrt{G}}{2}[\sqrt{G}\mathbf{\Omega}(1,1)\boldsymbol{\alpha}(\epsilon_0)\boldsymbol{\alpha}^H(\epsilon_0) \\ & - \boldsymbol{\alpha}(\epsilon_0)\mathbf{e}^T\mathbf{\Omega} - \mathbf{\Omega}\mathbf{e}\boldsymbol{\alpha}^H(\epsilon_0)], \\ E\{\delta\mathbf{u}_{\text{min}}\delta\mathbf{u}_{\text{min}}^T\} = & \frac{\sqrt{G}}{2}[-\sqrt{G}\Re\{\mathbf{\Omega}(1,1)\}\boldsymbol{\alpha}(\epsilon_0)\boldsymbol{\alpha}^T(\epsilon_0) \\ & + \mathbf{\Omega}\mathbf{e}\boldsymbol{\alpha}^T(\epsilon_0) + \boldsymbol{\alpha}(\epsilon_0)\mathbf{e}^T\mathbf{\Omega}^T], \end{aligned} \tag{75}$$

with $\mathbf{e} = [1, 0, \ldots, 0]^T$ and

$$\mathbf{\Omega} = \frac{\sigma_n^2}{Q-L}\sum_{g=2}^{G}\frac{\lambda_g+\sigma_n^2}{\lambda_g^2}\mathbf{u}_g\mathbf{u}_g^H \cong \frac{\sigma_n^2}{Q-L}\sum_{g=2}^{G}\frac{1}{\lambda_g}\mathbf{u}_g\mathbf{u}_g^H, \tag{76}$$

where $\{\lambda_g\}_{g=2}^G$ and $\{\mathbf{u}_g\}_{g=2}^G$ are the eigenvalues and eigenvectors of $\mathbf{R}_0$ not including the minimal eigenvalue and its associated eigenvector. The inequality in (76) holds when $\lambda_g \gg \sigma_n^2$ which occurs for large SNR. In this case we see that the variance of the estimate is linearly proportional to the noise variance, σ_n^2. Moreover, notice that the variance of the estimated CFO is inversely proportional to $\beta^2G^2/(Q-L)$, which is approximately inversely proportional to G^3/K, and this means that the variance inversely decreases w.r.t. the number of carriers. This concludes the derivation.

TABLE II
THE EFFECTIVE RANK, THE SQUARED NORMALIZED ERROR $\xi(\lambda_{\text{MIN}}) = |\lambda_{\text{MIN}}(\hat{\mathbf{R}}) - \lambda_{\text{MIN}}(\mathbf{R})|^2/\sigma_n^2$, AND SQUARED ERROR $\xi(\mathbf{u}_{\text{MIN}}) = \|\mathbf{u}_{\text{MIN}}(\hat{\mathbf{R}}) - \mathbf{u}_{\text{MIN}}(\mathbf{R})\|^2$

SNR [dB]	-10	-5	0	5	10	15
λ_1/λ_2	0.8011	0.5919	0.2969	0.1133	0.0382	0.0124
$\xi(\lambda_{\min})$	0.0173	0.0104	0.0092	0.0091	0.0090	0.0090
$\xi(\mathbf{u}_{\min})$	0.6412	0.0968	0.0189	0.0049	0.0015	0.0004

APPENDIX E
THE RANK OF THE MATRIX $\mathbf{R}_0$

In this Appendix we provide a proof that $\mathbf{R}_0$ has a rank equal to $G-1$ with probability (w.p.) one. By partitioning the $K \times 1$ vector $\mathbf{F}_K^H \mathbf{s}$ into G segments $\mathbf{s}_g = \mathbf{s}(g : g + (Q-1)G)$, $g = 0, 1 \ldots, G-1$ we can express the the gth segment $\{\mathbf{y}^{(g)}\}_{g=0}^{G-1}$ of $\mathbf{y}_0$ after simple algebraic steps as

$$\mathbf{y}^{(g)} = \sum_{g'=0}^{G-1} (\mathbf{H}_Q e^{j\frac{2\pi}{G}gg'} + \mathbf{\Delta}_L e^{j\frac{2\pi}{G}g(g'+1)})\mathbf{x}^{(g')}, \qquad (77)$$

where due to the structure of the matrix $\mathbf{H}$ we define the $Q \times Q$ matrices $\mathbf{H}_Q = \mathbf{H}(1:Q, 1:Q)$ and $\mathbf{\Delta}_L = \mathbf{H}(Q+1:2Q, 1:Q)$. Observe that $\mathbf{H}_Q$ is repeated along the main block diagonal of $\mathbf{H}$, while $\mathbf{\Delta}_L$ is repeated along the sub-block diagonal below the main block diagonal of $\mathbf{H}$. We also define the gth $Q \times 1$ vectors $\{\mathbf{x}^{(g)}\}_{g=0}^{G-1}$ as,

$$\mathbf{x}^{(g)} = \text{diag}(1, e^{j\frac{2\pi}{K}g}, \ldots, e^{j\frac{2\pi}{K}(Q-1)g})\mathbf{F}_Q^H \mathbf{s}^{(g)}. \qquad (78)$$

Notice that $\mathbf{x}^{(0)}$ is associated with the pilot symbols and in case of identical pilots we have,

$$\mathbf{H}_Q \mathbf{x}^{(0)} = u[\mathbf{h}^T, \mathbf{0}_{Q-L}^T]. \qquad (79)$$

Notice that $\mathbf{\Delta}_L$ has zero elements excepts at its first L rows and last L columns. Therefore, using (77) the matrix $\mathbf{Y}_0$ is written as,

$$\mathbf{Y}_0 = [\mathbf{0}_{Q-L}, \mathbf{H}_Q(L+1:Q, :)\underbrace{[\mathbf{x}^{(1)}, \cdots, \mathbf{x}^{(G-1)}]}_{\triangleq \mathbf{X}}]\mathbf{F}_G^H, \quad (80)$$

where $\mathbf{F}_G$ is the $G \times G$ matrix with the the (m,n)th element given by $\frac{1}{\sqrt{G}} e^{j\frac{2\pi}{G}mn}$. The matrix $\mathbf{H}_Q(L+1:Q, :)\mathbf{X}$ depends only on the data symbols and the channel. As the data symbols are randomly chosen, the probability that a set of data symbols generates a non full rank matrix is zero. We thus conclude that $\text{rank}(\mathbf{R}_0)$ is $G-1$ w.p. one.

To verify the above conclusion regarding the rank of $\mathbf{R}_0$ we examined the ratio between the minimal eigenvalue of $\hat{\mathbf{R}}$ and its second eigenvalue, the normalized squared error $\xi(\lambda_{\min}) = |\lambda_{\min}(\hat{\mathbf{R}}) - \lambda_{\min}(\mathbf{R})|^2/\sigma_n^2$, and the squared error $\xi(\mathbf{u}_{\min}) = \|\mathbf{u}_{\min}(\hat{\mathbf{R}}) - \mathbf{u}_{\min}(\mathbf{R})\|^2$ for different values of SNR. We used the model parameters detailed in Example 1 in Section IX for $G = 4$. Each result is averaged over 1000 Monte-Carlo trials. The results are presented in Table II. As can be seen, the results verify the previous conclusion regarding the effective rank of $\hat{\mathbf{R}}$, its minimal eigenvalue and its corresponding eigenvector. We simulated this example for higher values of G and obtained similar results.

ACKNOWLEDGMENT

The authors thank the Associate Editor and the anonymous reviewers for their time, effort, and important comments that helped to improve and clarify the paper.

REFERENCES

[1] Q. Zhan and H. Minn, "New integer normalized carrier frequency offset estimators," *IEEE Trans. Signal Process.*, vol. 63, no. 14, pp. 3697–3710, Jul. 2015.
[2] B. Xie, Q. Qiu, and H. Minn, "Exact signal model and new carrier frequency offset compensation scheme for OFDM," *IEEE Trans. Wireless Commun.*, vol. 11, no. 2, pp. 550–555, Feb. 2012.
[3] A. Salberg and A. Swami, "Doppler and frequency offset synchronization in wideband OFDM," *IEEE Trans. Wireless Commun.*, vol. 4, no. 6, pp. 2870–2881, Nov. 2005.
[4] P. H. Moose, "A technique for orthogonal frequency division multiplexing frequency offset correction," *IEEE Trans. Commun.*, vol. 42, no. 10, pp. 2908–2914, Oct. 1994.
[5] M. Ghogho and A. Swami, "Blind frequency-offset estimator for OFDM systems transmitting constant-modulus symbols," *IEEE Commun. Lett.*, vol. 6, no. 8, pp. 343–345, Aug. 2002.
[6] M. Ghogho and A. Swami, "Training design for multipath channel and frequency-offset estimation in MIMO systems," *IEEE Trans. Signal Process.*, vol. 54, no. 10, pp. 3957–3965, Oct. 2006.
[7] S. Zhou and Z. Wang, *OFDM for Underwater Acoustic Communications*. Hoboken, NJ, USA: Wiley, 2014.
[8] B. Li, M. Stojanovic, L. Freitag, and P. Willet, "Non uniform Doppler compensation for zero-padded OFDM over fast varying underwater acoustic channels," in *Proc. MTS/IEEE OCEANS Conf.*, 2007, pp. 1–6.
[9] B. Li, S. Zhou, M. Stojanovic, and L. Freitag, "Pilot based ZP-OFDM demodulation for an underwater acoustic channel," in *Proc. MTS/IEEE OCEANS Conf.*, Boston, MA, USA, Sep. 18–21, 2006, pp. 1–5.
[10] T. Kang and R. A. Iltis, "Iterative carrier frequency offset and channel estimation for underwater acoustic OFDM systems," *IEEE J. Sel. Areas Commun.*, vol. 26, no. 9, pp. 1650–1661, Dec. 2008.
[11] B. Li, S. Zhou, M. Stojanovic, L. Freitag, and P. Willett, "Multicarrier communication over underwater acoustic channels with nonuniform Doppler shifts," *IEEE J. Ocean. Eng.*, vol. 33. no. 2, pp. 198–209, Apr. 2008.
[12] P. C. Carrascosa and M. Stojanovic, "Adaptive channel estimation and data detection for underwater acoustic MIMO-OFDM systems," *IEEE J. Ocean. Eng.*, vol. 35, no. 3, pp. 635–646, Jul.2010.
[13] F. Classen and H. Meyer, "Frequency synchronization algorithms for OFDM systems suitable for communication over frequency selective fading channels," in *Proc. IEEE 44th Veh. Technol. Conf.*, Stockholm, Sweden, Jan. 8–10, 1994, pp. 1655–1659.
[14] T. M. Schmidl and D. C. Cox, "Robust frequency and timing synchronization for OFDM," *IEEE Trans. Commun.*, vol. 45, no. 12, pp. 1613–1621, Dec. 1997.
[15] M. Morelli and U. Mengali, "Carrier frequency estimation for transmissions over selective channels," *IEEE Trans. Commun.*, vol. 48, no. 9, pp. 1580–1589, Sep. 2000.
[16] S. Attallah, "Blind estimation of residual carrier offset in OFDM systems," *IEEE Signal Process. Lett.*, vol. 11, no. 2, pp. 216–219, Feb. 2004.
[17] M. Luise, M. Marselli, and R. Reggiannini, "Low complexity blind carrier frequency recovery for OFDM signals over frequency selective radio channels," *IEEE Trans. Commun.*, vol. 50, no. 7, pp. 1182–1188, Jul. 2002.
[18] X. Ma, C. Tepedelenlioglu, G. B. Giannakis, and S. Barbarossa, "Non-data-aided carrier offset estimations for OFDM with null subcarriers: Identifiability, algorithms, and performance," *IEEE J. Sel. Areas Commun.*, vol. 19, no. 12, pp. 2504–2515, Dec. 2001.
[19] Y. Yao and G. B. Giannakis, "Blind carrier frequency offset estimation in SISO, MIMO, and multiuser OFDM systems," *IEEE Trans. Commun.*, vol. 53, no. 1, pp. 173–183, 2005.
[20] J. J. van de Beek, M. Sandell, and P. O. Borjesson, "ML estimation of time frequency in OFDM systems," *IEEE Trans. Signal Process.*, vol. 45. no. 7, pp. 1800–1805, Jul.1997.
[21] N. Lashkarian and S. Kiaei, "Class of cyclic based estimators for frequency offset estimation of OFDM systems," *IEEE Trans. Commun.*, vol. 48, no. 12, pp. 2139–2149, Dec. 2000.

[22] U. Tureli, H. Liu, and M. D. Zoltowski, "OFDM blind carrier offset estimation: ESPRIT," *IEEE Trans. Commun.*, vol. 48, no. 9, pp. 1459–1461, Sep. 2000.
[23] M. Morelli and U. Mengali, "An improved frequency offset estimator for OFDM applications," *IEEE Commun. Lett.*, vol. 3, no. 3, pp. 75–77, Mar. 1999.
[24] W. Zhou, Z. H. Wang, J. Huang, and S. Zhou, "Blind CFO estimation for zero-padded OFDM over underwater acoustic channels," in *Proc. MTS/IEEE OCEANS Conf.*, Kona, Hawaii, Sep. 2011, pp. 1–7.
[25] M. Stojanovic and J. Preisig, "Underwater acoustic communication channels: Propagation models and statistical characterization," *IEEE Commun. Mag.*, vol. 47, no. 1, pp. 84–89, Jan. 2009.
[26] B. Muquet, Z. Wang, G. B. Giannakis, M. de Courville, and P. Duhamel, "Cyclic prefix or zero padding for multicarrier transmission?" *IEEE Trans. Commun.*, vol. 50, no. 12, pp. 2136–2148, Dec. 2002.
[27] H. C. So, Y. T. Chan, K. C. Ho, and Y. Chen, "Simple formulas for bias and mean error computation," *IEEE Signal Process. Mag.*, vol. 30, no. 4, pp. 162–165, Jul.2013.
[28] P. Qarabaqi and M. Stojanovic, "Statistical characterization and computationally efficient modeling of a class of underwater acoustic communication channels," *IEEE J. Ocean. Eng.*, vol. 38. no. 4, pp. 701–717, Oct. 2013.
[29] B. Friedlander and A. J. Weiss, "On the second order statistics of the eigenvectors of sample covariance matrices," *IEEE Trans. Signal Process.*, vol. 46, no. 11, pp. 3136–3139, Nov. 1998.
[30] G. A. Sitton, C. S. Burrus, J. W. Fox, and S. Treitel, "Factoring very high degree polynomials," *IEEE Signal Process. Mag.*, vol. 20, no. 6, pp. 27–42, Nov. 2003.
[31] H. L. Van Trees, *Optimum Array Processing*. Hoboken, NJ, USA: Wiley, 2001.
[32] J. W. Demmel, *Applied Numerical Linear Algebra*. Philadelphia, PA, U.S.A: SIAM, 1997.
[33] P. M. Duric and S. M. Kay, "Parameter estimation of chirp signals," *IEEE Trans. Acoust., Speech, Signal Process.*, vol. 38, no. 12, pp. 2118–2126, Dec. 1990.
[34] A. Amar, A. Leshem, and A. J. van-der Veen, "A low complexity blind estimation of narrowband polynomial phase signals," *IEEE Trans. Signal Process.*, vol. 58, no. 9, pp. 4674–4683, Sep. 2010.
[35] Y. Doweck, A. Amar, and I. Cohen, "Joint model order selection and parameter estimation of chirps with harmonic components," *IEEE Trans. Signal. Process.*, vol. 63, no. 7, pp. 1765–1778, Apr. 2015.
[36] R. J. Vaccaro, "A second order perturbation expansion for the SVD," *SIAM J. Mater. Anal. Appl.*, vol. 15, no. 2, pp. 661–671, Apr. 1994.

Alon Amar (S'04–M'09) received the B.Sc. degree in electrical engineering from the Technion-Israel Institute of Technology, Haifa, Israel, in 1997 and the M.Sc. degrees in electrical engineering from Tel Aviv University, Tel Aviv, Israel, in 2003, and 2009, respectively. From 2009 to 2010, he was a Postdoctoral Research Associate with the Circuits and Systems group, Faculty of Electrical Engineering, Mathematics, and Computer Science, Delft University of Technology, Delft, The Netherlands. In 2011, he joined the Israeli National Research Center, Haifa, as a Research Scientist. Since 2016, he is an Adjunct Lecturer and a Research Associate in the Department of Electrical Engineering, Technion, Israel Institute of Technology. His main research interests include statistical and array signal processing, wireless communication, and sensor networks.

Gilad Avrashi (S'16) received the B.S degree in electrical engineering from the Technion Israel institute of technology, Haifa, Israel, in 2013, where he is currently working toward the Graduate degree in the Faculty of Electrical Engineering. His main research interests include signal processing, wireless communications, and sensor networks and their applications for underwater acoustics systems. Since 2015, he leads the underwater acoustic communication group in the Israeli National Research Center, Haifa, Israel. The group conducts academic research as well as sea trials and full scale development of underwater modems.

Milica Stojanovic (SM'08–F'10) received the Graduate degree from the University of Belgrade, Belgrade, Serbia, in 1988, and the M.S. and Ph.D. degrees in electrical engineering from Northeastern University, Boston, MA, USA, in 1991 and 1993, respectively. She was a Principal Scientist at MIT, and in 2008, she joined Northeastern University, where she is currently a Professor of electrical and computer engineering. She is also a Guest Investigator at the Woods Hole Oceanographic Institution and a Visiting Scientist at MIT. She received the 2015 IEEE/OES Distinguished Technical Achievement Award. Her research interests include digital communications theory, statistical signal processing, and wireless networks and their applications to underwater acoustic systems. She is an Associate Editor for the IEEE JOURNAL OF OCEANIC ENGINEERING and a past Associate Editor for IEEE TRANSACTIONS ON SIGNAL PROCESSING and IEEE TRANSACTIONS ON VEHICULAR TECHNOLOGY. She also serves on the Advisory Board of IEEE Communication Letters and chairs the IEEE Ocean Engineering Societys Technical Committee for Underwater Communication, Navigation, and Positioning.